

A collicular map for touch-guided tongue control

<https://doi.org/10.1038/s41586-024-08339-3>

Brendan S. Ito^{1,2}✉, Yongjie Gao^{1,2}, Brian Kardon¹ & Jesse H. Goldberg¹✉

Received: 8 April 2024

Accepted: 4 November 2024

Published online: 1 January 2025

 Check for updates

Accurate goal-directed behaviour requires the sense of touch to be integrated with information about body position and ongoing motion^{1,2}. Behaviours such as chewing, swallowing and speech critically depend on precise tactile events on a rapidly moving tongue³, but neural circuits for dynamic touch-guided tongue control are unknown. Here, using high-speed videography, we examined three-dimensional lingual kinematics as mice drank from a water spout that unexpectedly changed position during licking, requiring re-aiming in response to subtle contact events on the left, centre or right surface of the tongue. Mice integrated information about both precise touch events and tongue position to re-aim ensuing licks. Touch-guided re-aiming was unaffected by photoinactivation of tongue sensory, premotor and motor cortices, but was impaired by photoinactivation of the lateral superior colliculus (latSC). Electrophysiological recordings identified latSC neurons with mechanosensory receptive fields for precise touch events that were anchored in tongue-centred, head-centred or conjunctive reference frames. Notably, latSC neurons also encoded tongue position before contact, information that is important for tongue-to-head-based coordinate transformations underlying accurate touch-guided aiming. Viral tracing revealed tongue sensory inputs to the latSC from the lingual trigeminal nucleus, and optical microstimulation in the latSC revealed a topographic map for aiming licks. These findings demonstrate that touch-guided tongue control relies on a collicular mechanosensorimotor map, analogous to collicular visuomotor maps associated with visually guided orienting across many species.

If your little finger nicks your coffee cup as you extend your arm to reach for it, you immediately reposition your fingers laterally to optimally grasp and lift the cup. Similarly, as you eat and drink, tactile feedback enables your tongue to dexterously handle food and water for chewing and swallowing while maintaining airway patency and preventing tongue injury. Impairments in the tongue's ability to handle food and water result in aspiration pneumonia, a leading cause of death in neurological disease⁴. Just as fingertip anaesthesia impairs grasping even with visual feedback intact^{5,6}, blockade of tactile feedback to the tongue impairs chewing, swallowing and speech³. Yet the neural circuits underlying touch-guided tongue control remain unclear.

Touch guides ongoing tongue movements

To test whether mice use tactile feedback for tongue control, we developed a touch-guided lick task that requires mice to re-aim licks in response to subtle contact events on the tongue surface. We first trained head-fixed mice to withhold licking for 1 s to receive an auditory cue, and to contact a water spout aligned to the centre of the facial midline within 1.3 s to earn a water reward. Mice naturally lick in rhythmic bouts of 4–8 licks at around 8 Hz (ref. 7). We detected spout contacts in real time and randomly displaced the spout to the left or

right by approximately one half of the tongue width (1.1 mm on average) between the first (L1) and second (L2) licks of a bout (Fig. 1a and Methods; around 400 trials per session; spout moved to left, centre or right positions with equal probability). Importantly, the subtle spout displacements between L1 and L2 did not cause spout misses on L2 but instead evoked unexpected nicks at distinct locations on the tongue surface (Fig. 1b–d).

To precisely quantify both three-dimensional (3D) tongue kinematics and nick sites, we combined dual-plane kilohertz-frame-rate tongue imaging, deep-learning-based image segmentation and visual hull reconstruction to estimate the tongue 3D volume and tip position in each frame, resulting in millisecond-resolution tongue-tip trajectories for each lick⁸ (Fig. 1b and Methods). Next, to determine the precise location on the tongue surface that contacted the spout on each lick, we embedded a 3D model of the spout in the same space as the 3D hull reconstruction of the tongue, and identified the centroid of the reconstructed tongue voxels that neighboured or overlapped with spout voxels (Fig. 1b and Methods). We defined a fiducial point at the base of the jaw that defined the midline of each animal, and then quantified the spout–tongue contact site on each lick as the angle between two vectors: from the fiducial point to the tongue tip (that is, the tip vector) and the fiducial point to the contact centroid (that is, the

¹Department of Neurobiology and Behavior, Cornell University, Ithaca, NY, USA. ²These authors contributed equally: Brendan S. Ito, Yongjie Gao. ✉e-mail: itobrendan@gmail.com; jessehgoldberg@gmail.com

Article

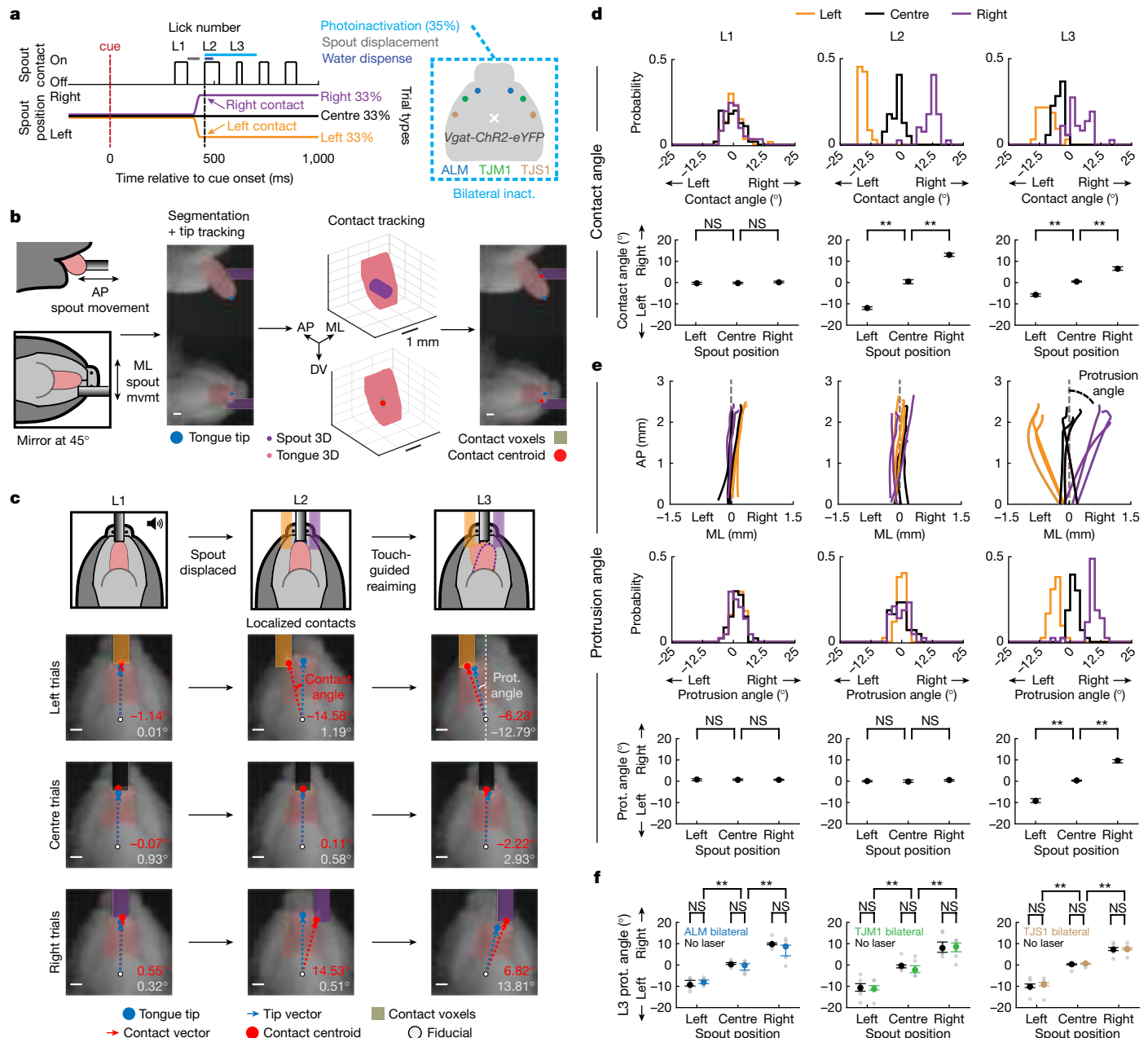


Fig. 1 | Lingual cortical areas are not required for touch-guided re-aiming.

a, The trial structure (left). An initially centred water spout was randomly moved to the centre, left or right positions between the first (L1) and second (L2) licks of a bout. On 35% of trials, L2 contact triggers laser on (250 ms). Right, optical fibres were implanted bilaterally over the ALM, TJM1 or TJS1 in VGAT-ChR2-eYFP mice. Inact., inactivation. **b**, Schematic and still frame of L2 contact on a spout-right (purple) trial (left). Side and bottom views were filmed (1 kHz frame rate), two convolutional neural networks segmented the tongue (pink mask) and the tongue tip location (blue dot) was computed from the 3D hull tongue reconstruction on each frame. Right, the contact centroid (red dot) was defined as the centroid of all contact voxels (brown mask). DV, dorsoventral; ML, mediolateral; mvmt, movement. **c**, Bottom-view still frames at L1–L3 contact onset across trial types. The contact site was defined as the angle between the tip vector (blue dashed line, fiducial to the tongue tip) and contact vector (red dashed line, fiducial to the contact centroid). The protrusion (prot.) angle was defined as the angle between the tip vector and facial midline. **d**, L1–L3 contact angle distributions on left (gold), centre (black) and right (purple) trials for a single session (top). Bottom, L1–L3 contact angles across mice ($n = 14$ mice). **e**, Example L1–L3 tongue tip protrusion trajectories (top). Middle and bottom, the same as **d**, except for L1–L3 protrusion angles. **f**, L3 re-aiming was intact during photoinactivation of the ALM, TJM1 and TJS1. L3 protrusion angles for no-laser (black) trials and ALM (blue, $n = 7$ mice), TJM1 (green, $n = 6$ mice) and TJS1 (brown, $n = 6$ mice) inactivation trials. Grey dots show the median values of individual mice. For **d–f**, data are median \pm IQR. Statistical analysis was performed using two-sided hierarchical bootstrap test; **corrected $P < 0.01$; NS, not significant. Exact statistical values are provided in Supplementary Tables 1 and 3. Panels **b** and **c** were adapted from ref. 8, Springer Nature Limited. Scale bars, 1 mm (**b** and **c**).

and contact vector (red dashed line, fiducial to the contact centroid). The protrusion (prot.) angle was defined as the angle between the tip vector and facial midline. **d**, L1–L3 contact angle distributions on left (gold), centre (black) and right (purple) trials for a single session (top). Bottom, L1–L3 contact angles across mice ($n = 14$ mice). **e**, Example L1–L3 tongue tip protrusion trajectories (top). Middle and bottom, the same as **d**, except for L1–L3 protrusion angles. **f**, L3 re-aiming was intact during photoinactivation of the ALM, TJM1 and TJS1. L3 protrusion angles for no-laser (black) trials and ALM (blue, $n = 7$ mice), TJM1 (green, $n = 6$ mice) and TJS1 (brown, $n = 6$ mice) inactivation trials. Grey dots show the median values of individual mice. For **d–f**, data are median \pm IQR. Statistical analysis was performed using two-sided hierarchical bootstrap test; **corrected $P < 0.01$; NS, not significant. Exact statistical values are provided in Supplementary Tables 1 and 3. Panels **b** and **c** were adapted from ref. 8, Springer Nature Limited. Scale bars, 1 mm (**b** and **c**).

contact vector) (Fig. 1c). We chose an angular coordinate system because it captures tongue contact site variance in both the mediolateral and anteroposterior axes with a single term (Methods). Together, these methods enabled us to track both nick sites and lick kinematics with millisecond precision.

In all of the mice tested, left or right nicks on L2 (Fig. 1d) caused immediate re-aiming of the next lick (L3; Fig. 1e, Supplementary Video 1 and Methods), suggesting that mice naturally use touch to guide tongue aiming within lick bouts. Touch-guided re-aiming did not depend on water dispensation at contact (Extended Data Fig. 1), and the rhythm of

the lick bout was not affected by the process of touch-guided re-aiming (Extended Data Fig. 2a), showing that the sensorimotor process linking tactile feedback circuits to premotor tongue steering circuits occurs rapidly, within a single inter-lick interval (median latency from L2 contact onset to L3 protrusion onset, 141 ms (interquartile range (IQR) = 127–148 ms); $n = 14$ mice).

Re-aiming does not require lingual cortical areas

Touch-guided grasping and visually guided reaching depend on sensory and motor cortical processing^{9,10}. Three sensorimotor lingual cortical areas—the tongue–jaw sensory cortex (TJS1), tongue–jaw motor cortex (TJM1) and anterolateral motor cortex (ALM)—are implicated in diverse lick aiming tasks^{8,11,12}. To test whether touch-guided tongue aiming similarly requires cortical pathways, we used VGAT-ChR2-eYFP mice to bilaterally photoinhibit the TJS1, TJM1 or ALM^{8,11,12}. Photoinhibition for each region was initiated at the moment of L2 spout contact on 35% of trials and lasted for 250 ms, ensuring inhibition from L2 contact to L3 re-aiming (Fig. 1a, Extended Data Fig. 3a–d and Methods). Licks produced during ALM and TJM1 inactivation exhibited reduced durations and pathlengths (Extended Data Fig. 2e–j), consistent with past reports^{8,11}, suggesting that photoinhibition effectively impaired the function of the relevant brain regions. Notably, however, touch-guided re-aiming on L3 was completely intact both during photoinactivation of the TJS1, TJM1 and ALM (Fig. 1f and Supplementary Video 2) and after complete bilateral lesion of all three areas at once (Extended Data Fig. 4 and Supplementary Video 3), suggesting that lingual cortical areas are not required for touch-guided tongue aiming.

The latSC is important for re-aiming

Across vertebrates, the superior colliculus (SC) is involved in stimulus-guided orienting^{13–16}. The SC receives direct visual input from the retina¹⁴ and contains a topographically organized visuomotor map in which each region of the visual field maps to a corresponding territory in the contralateral SC^{17–20}. We hypothesized that a lateral region of the SC (latSC) recently associated with directional licking^{21,22} may be analogously important for touch-guided tongue control.

To test the role of the latSC in touch-guided tongue aiming, we used *Vgat-cre* mice to express channelrhodopsin-2 (ChR2) in GABAergic inputs to the latSC from the substantia nigra pars reticulata (SNr) and implanted optic fibres over the latSC. This approach was shown to inhibit latSC discharge and impair licking in previous research²¹. We bilaterally photoinhibited the latSC by photoactivating SNr terminals in the latSC from L2 contact onset through the entire duration of L3 on 35% of trials (Figs. 1a and 2a, Extended Data Fig. 3e,f and Methods). In contrast to inactivation of the ALM, TJS1 or TJM1, bilateral latSC inactivation immediately interrupted lick bouts (Fig. 2b, Extended Data Fig. 2b–d and Supplementary Video 4), consistent with previous research²¹.

We reasoned that unilateral inactivation experiments may help to clarify the precise role of the latSC in touch-guided re-aiming. In our task, tactile signals from L2 nicks must somehow reach tongue steering circuits before L3. Any interruption of this sensorimotor path may block touch-guided re-aiming on L3. Unilateral inactivations of multiple brain regions, including the TJM1, ALM or latSC, are all known to cause an ipsilateral steering bias^{12,22}. Thus, if any one of these brain regions can contribute to lick aiming but is not necessary for reacting to the touch event, then unilateral inactivation of that region during and after the L2 nick should bias all L3 protrusions ipsilaterally, without eliminating re-aiming due to the L2 nick event. Therefore, over a session of left, centre and right spout contacts on L2 with unilateral photoinactivation in those regions, three distinct peaks in the L3 protrusion angle distributions would still exist on both intact and unilateral inactivation trials, but the peaks with unilateral inactivation would all be biased

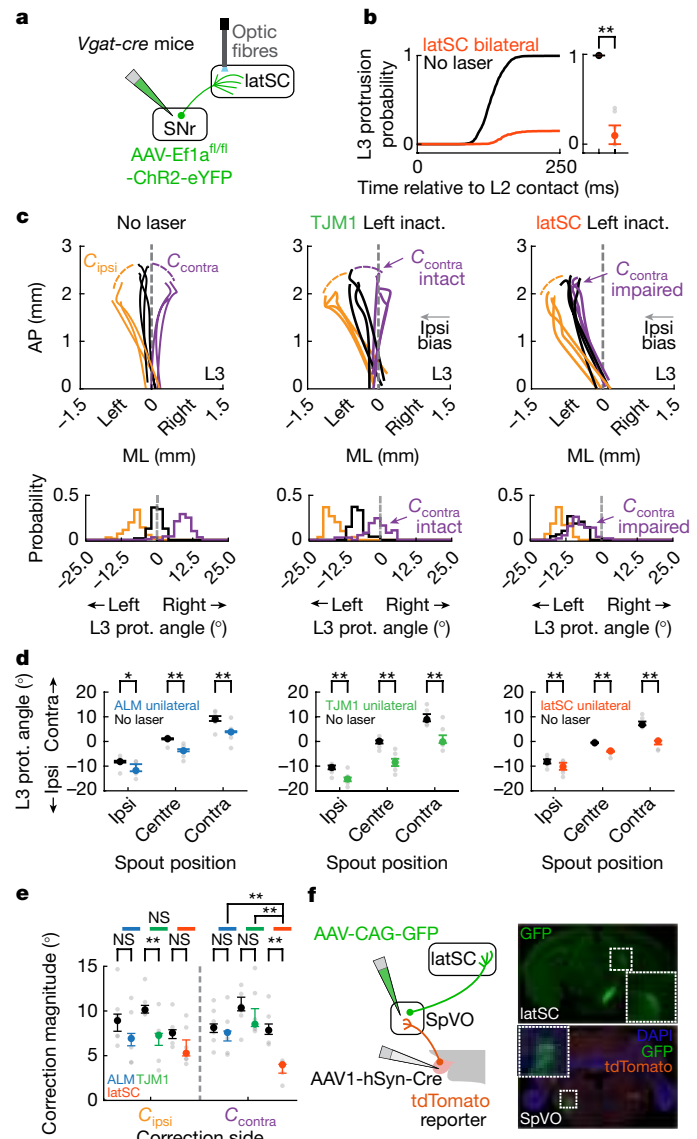


Fig. 2 | Photoinactivation of the latSC impairs touch-guided re-aiming.

a, The latSC photoinhibition strategy. Photoinhibition timing was performed as in Fig. 1a. **b**, The cumulative L3 protrusion probability for no-laser (black) and latSC-inactivated (red-orange) trials across mice (left). Right, the L3 protrusion probability. $n = 6$ mice. **c**, Example L3 protrusion trajectories (top) and protrusion angle distributions (bottom) from single sessions for no-laser (left) trials, and left TJM1 (centre) or latSC (right) inactivation trials. Contralateral (C_{contra}) and ipsilateral (C_{ipsi}) corrections on L3 were defined as the difference in the median protrusion angle between the centre and contralateral, or ipsilateral, trials for each mouse. Unilateral activations could have no effect, could cause an ipsilateral steering bias across all trial types but preserve corrections, or could cause both an ipsilateral bias and impair contralateral corrections on L3. Note that C_{contra} and C_{ipsi} were preserved with left TJM1 inactivation, whereas left latSC inactivation specifically impaired C_{contra} . **d**, L3 protrusion angles for laser-off (black) and laser-on trials; unilateral ALM (blue, $n = 7$), TJM1 (green, $n = 6$) and latSC (red-orange, $n = 6$). Note that all inactivations caused an ipsilateral bias. **e**, C_{contra} and C_{ipsi} re-aiming magnitudes for ALM, TJM1 and latSC photoinactivations. Colours are as in **d**. Note that latSC photoinactivation specifically impaired C_{contra} . **f**, Tracing schematic (left). Right, axonal projections from the SpVO to the latSC (top, green) and axonal projections from the primary trigeminal to the SpVO (bottom, orange) with GFP-labelled SpVO cell bodies (green). For **b**, **d** and **e**, data are median \pm IQR. The grey dots in **d** and **e** represent the median values of individual mice. Statistical analysis was performed using two-sided hierarchical bootstrap tests; *corrected $P < 0.05$. Exact statistical values are provided in Supplementary Tables 4, 7 and 8. Panel **f** was adapted from ref. 8, Springer Nature Limited.

ipsilaterally towards the inactivated side (Fig. 2c (compare the left and middle panels)). This outcome would suggest that, while the inactivated brain region can contribute to tongue steering, a distinct circuit is driving the touch-guided re-aiming process. On the other hand, if a brain region is an essential part of the touch-to-steering circuit, then unilateral inactivation of that region might block the ability to re-aim in response to contralateral, but not ipsilateral, nicks^{22,23}. As a result, the peak representing contralateral trials would largely merge with the peak for centre trials, leaving only two peaks (Fig. 2c (compare the left and right panels)). This result would also suggest that other steering circuits may not be sufficient to implement contralateral touch-guided corrections on their own.

We performed unilateral photoactivation of the ALM, TJM1 or latSC in separate batches of mice with the same duration and timing as bilateral photoactivation to test these hypotheses. We defined the correction magnitude for each animal as the difference between the median L3 protrusion angle for the centre condition and the median L3 protrusion angle for either the contralateral or ipsilateral condition, which were defined relative to the inactivated hemisphere to enable comparisons. Unilateral ALM, TJM1 and latSC inactivations minimally impaired L3 lick kinematics (Extended Data Fig. 5) and, as expected, biased licks ipsilaterally^{23–25} (Fig. 2c,d and Supplementary Video 5). Critically, however, unilateral latSC, but not ALM or TJM1, inactivation selectively impaired contralateral re-aiming, while preserving ipsilateral re-aiming (Fig. 2c–e, Supplementary Video 6 and Supplementary Table 8; 4.0° (IQR = 3.1–4.5°) median magnitude of contralateral correction with unilateral latSC inactivation, 7.9° (IQR = 7.4–8.6°) for the control). Notably, this result resembles impairments from unilateral SC inactivations in saccade tasks, in which orienting to contralateral visual targets is specifically impaired^{24,25}. These findings suggest that the latSC is part of the neural pathway that links tactile information from L2 to re-aiming commands for L3.

A pathway from the tongue to the latSC

If the latSC is involved in processing touch signals from the tongue to guide next lick aiming, then the latSC should receive input from tongue sensory afferents. To test this idea, we performed viral tracing experiments with tongue injections. Oral sensory neurons reside in the primary trigeminal ganglion and project to secondary trigeminal nuclei in the brainstem²⁶. To test whether the latSC receives input from secondary trigeminal nuclei that, in turn, receive input from primary tongue trigeminal neurons, we injected a Cre-expressing adeno-associated virus (AAV) into the tongues of *Rosa26^{LSL-dTomato}* mice to fluorescently label primary trigeminal neurons innervating the tongue. We identified axon terminals in the dorsal subdivision of spinal trigeminal nucleus oralis (SpVO), a secondary trigeminal region that is known to project to the hypoglossal nucleus and the latSC, suggesting a role in touch-guided tongue control^{27–29}. We next injected a GFP-expressing AAV into this part of the SpVO and identified projections to the contralateral latSC (Fig. 2f; $n = 3$ mice). The finding that the latSC receives input from a lingual territory of the SpVO raises the possibility that the latSC might process tactile feedback to guide ongoing licking.

The latSC encodes lingual contact events

To test for possible roles of the latSC in processing tactile feedback, we recorded latSC neural activity during the touch-guided lick task ($n = 553$ neurons, 64 sessions, 6 mice). Many latSC neurons exhibited touch-site-dependent (left, centre, right) changes in activity during the first 100 ms after L2 contact (Fig. 3a,b, Extended Data Fig. 6a,b and Methods; $n = 279$ out of 553 neurons), with most touch-sensitive neurons selective for contralateral contacts (Fig. 3b,c, Extended Data Fig. 6a,b and Methods; $n = 184$ out of 279 neurons with significant contralateral selectivity). The relative proportion of neurons with

contralateral contact selectivity was significantly higher at posterior versus anterior latSC recording locations (Fig. 3c and Supplementary Tables 9 and 10), suggesting that selectivity is graded along the anteroposterior axis in the latSC. Notably, a similar anteroposterior gradient for nasal to temporal visual selectivity is observed in the SC of many species^{13–15,30}.

We wondered whether the precise location of contact events on the subregions of the tongue surface sampled in our task influenced latSC discharge in neurons responsive to L2 contact. We visualized tuning to contact locations by plotting the firing rate of single latSC neurons after L2 contact against L2 contact angle (Fig. 3a (bottom) and Methods), defined as the angle between the tip vector and the contact vector at the moment of spout contact. We assessed the significance of receptive fields in two ways. First, we computed a mutual information metric that quantifies site-specific contact information present in spikes. Using this metric, 42% of all neurons significantly encoded contact angle information ($n = 179$ out of 422; Fig. 3d), with some neurons exhibiting highly selective responses (Fig. 3a (left and middle)). Second, we correlated latSC single-unit firing rates with L2 contact angle (Fig. 3a (bottom)) and found that 34% ($n = 143$ out of 422) of neurons that were modulated after L2 contact exhibited significant tuning, including many with very strong linear fits (Fig. 3e and Methods). Together, these complementary analyses show that latSC neurons can exhibit precise tactile responses to tongue contacts and exhibit significant selectivity for contact angle. The diverse range of tuning widths for contact angle resembles the variation in receptive field sizes previously observed for visual and auditory stimuli in the rodent SC^{18,31,32}.

Principal component analysis (PCA) of latSC population activity showed that neural trajectories after left or right contacts significantly diverged rapidly from the neural trajectory after centre contacts (Fig. 3f and Methods; 35 ms after contact (IQR = 30–35 ms)). Notably, contact response latencies were faster in individual latSC neurons (mode of neuronal latency distribution, 16 ms; Fig. 3g and Methods). Thus contact representations arose during L2 contact (median L2 contact duration, 61 ms (IQR = 47–73 ms)) and well before the initiation of L3 (median latency from L2 contact to L2 retraction offset, 69.5 ms (IQR = 49.5–80 ms); median latency from L2 contact to L3 protrusion onset, 141 ms (IQR = 127–148 ms)).

To test the behavioural relevance of these fine-scale tactile representations, we plotted the magnitude of L3 re-aiming against the precise contact angle on L2 and identified a very strong correlation that was significant both within and across trial types (Extended Data Fig. 7). Larger L2 contact angles resulted in larger protrusion angle changes between L2 and L3 (Extended Data Fig. 7c–f), even for only slightly off-centre nicks (Extended Data Fig. 7e), demonstrating that mice used the precise locations of nick sites on L2 to adjust their aim for L3.

Tactile reference frames in the latSC

For tactile feedback to be transformed to an estimate of spout position for aiming the next lick, a mouse might need to know not only where on the tongue surface the contact occurred but also the position of the tongue at the moment of contact. For example, a left nick during a straight lick specifies a spout to the left of the head, but the same left nick during a right-aimed lick specifies a centred spout. Touch-based re-aiming may require a coordinate transformation from a tongue- to a head-based reference system.

To examine the coordinate systems for lingual contact representations, we created a ‘recentering’ task that decouples the nick site from the spout position. In this task, we produced left/right spout displacements on L2 that were followed by recentring spout displacements between L3 and L4 on 35% of trials (Fig. 4a). Mice reliably used L4 contacts to re-aim L5, showing that nicks on laterally aimed licks can cause re-aiming to centre (Fig. 4b and Supplementary Video 7). Note that tongue- and head-based reference frames make distinct predictions

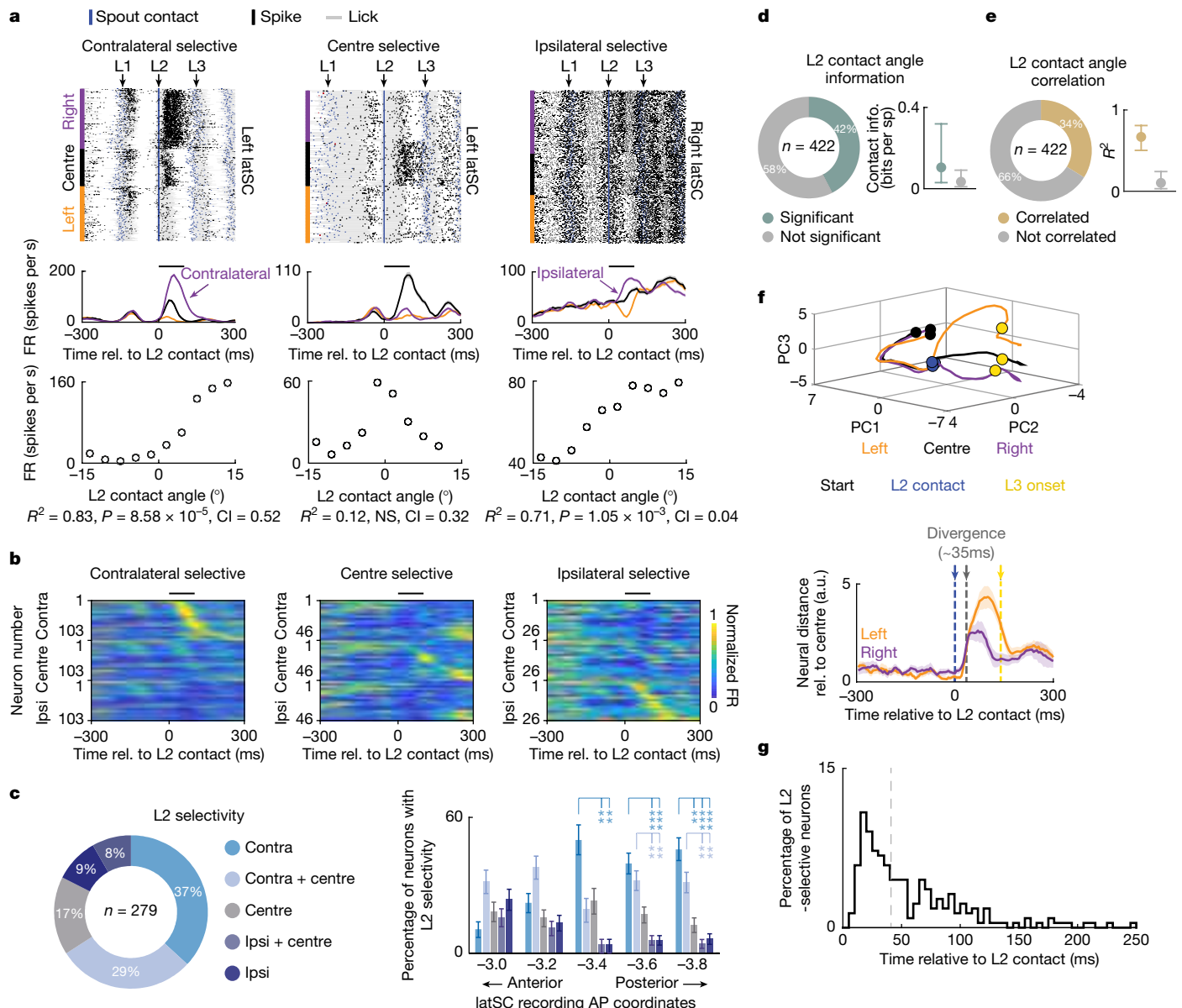


Fig. 3 | latSC neural activity encodes the location of contact events on the tongue surface. **a**, Spike rasters (top row) and rate histograms (middle row) from example latSC neurons selective for contralateral (left), centre (middle) or ipsilateral (right) L2 contacts. Rasters are sorted by condition, then by L2 contact angle within each condition. Colours are as in Fig. 1a. Shading represents the bootstrapped s.e.m. across trials. The black bar shows the spike window (100 ms) used to assess firing rate differences. Bottom row, the relationship between the L2 contact angle (3° bins) and the mean binned firing rate (FR). CI, contact angle information (bits per spike); rel., relative. **b**, Normalized mean firing rates of latSC neurons selective for contralateral (left, $n = 103$ out of 279), centre (middle, $n = 46$ out of 279) or ipsilateral (right, $n = 26$ out of 279) L2 contacts (Methods). **c**, The percentage (left) and AP distribution (right; Methods) of L2 contact-modulated neurons selective for contralateral (cyan, $n = 103$), contralateral and centre (light blue, $n = 81$), centre (grey, $n = 46$), ipsilateral (dark blue, $n = 26$), and ipsilateral and centre (blue, $n = 23$) contacts. The error bars show the bootstrapped IQR.

Statistical analysis was performed using two-sided bootstrap tests; ***corrected $P < 0.001$. **d**, The percentage of L2 contact-modulated neurons with significant contact angle information (info.; CI, green). Right, the median \pm IQR of contact angle information in bits per spike across neurons with significant contact angle information. **e**, The percentage of L2 contact-modulated neurons correlated with L2 contact angle (gold) (left). Right, median \pm IQR R^2 across L2 contact-angle-correlated neurons. **f**, First three principal components (PCs) of condition-averaged latSC population activity (top). Bottom, the Euclidean distance between the neural trajectories for left (gold) and right (purple) trials relative to centre trials. Shading represents the bootstrapped s.e.m. **g**, latSC single-neuron divergence latencies for L2 selective neurons (Methods). The grey dashed line shows the median (41 ms); mode, 16 ms. For **a**, **b**, **f** and **g**, data are aligned to L2 contact onset. Recording sites and exact statistical values are provided in Supplementary Tables 9 and 10, respectively.

for neural responses to L2 and L4 contacts in the recentering task. A tongue-centric frame would encode the position of the nick site in a coordinate system anchored to the tongue, which would predict similar nick-site selectivity on L2 and L4, even for nicks specifying distinct spout locations relative to the head (Fig. 4c (top)). By contrast, a head-centric frame would encode the position of the spout in space relative to the head, which would require tactile responses to be

integrated with information about the position of the entire tongue at the moment of contact (Fig. 4d (top)).

To determine whether contact representations depended on tongue position, we first noted that many neurons exhibited selectivity for contacts on specific licks in the bout (Extended Data Fig. 8a–f). We identified neurons during recentering sessions that exhibited nick site-selective responses to both L2 and L4 (Extended Data Fig. 8c;

Article

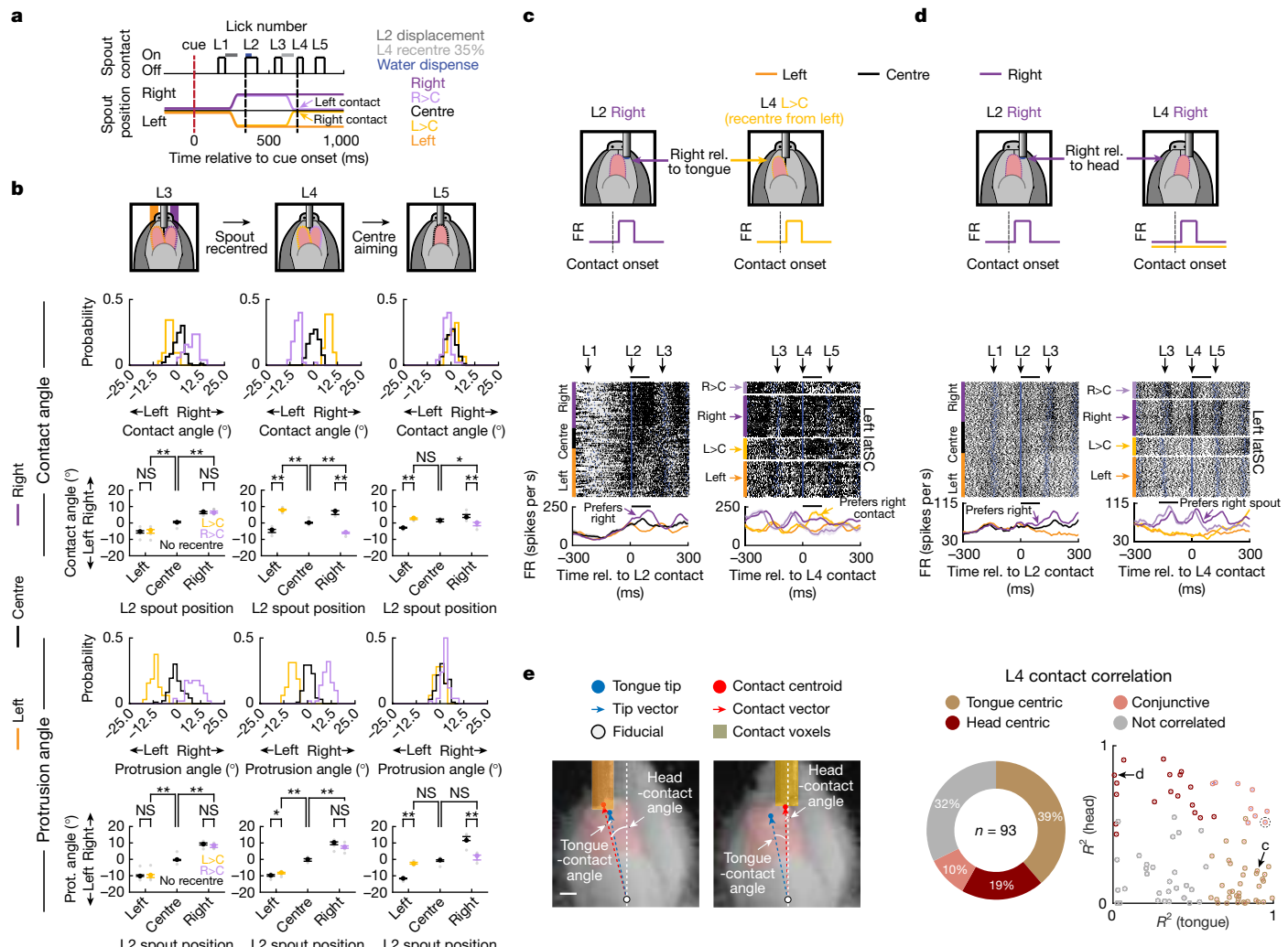


Fig. 4 | latSC neurons encode contact location in tongue-centric, head-centric and conjunctive coordinate frames. **a**, The trial structure in recentring sessions. The spout was randomly returned from the left or right (35%) back to the centre position between L3 and L4. Recentring sessions had five trial types: the spout could remain left (orange), centre (black) or right (purple), or the spout could return from left to centre ($L>C$, light orange) or from right to centre ($R>C$, light purple). On L4, $L>C$ trials evoke right nicks and $R>C$ trials evoke left nicks. **b**, Schematic of L3–L5 contacts and re-aiming on recentring trials (top). Middle, L3–L5 contact angle histograms (top) from an example session and the median \pm IQR across mice (bottom, $n = 5$). Bottom, the same as for the top plots, but for L3–L5 protrusion angles. Lateralized L4 contacts lead to centre re-aiming on L5. **c**, Illustration of a tongue-centric neuron activated by the same contact location on L2 and L4 (top). Bottom, spike rasters and rate histograms for an example latSC neuron aligned to L2 (left) and

L4 contact (right). This neuron was activated by right-relative-to-tongue contacts (tongue centric) on both L2 (right trials) and L4 ($L>C$ trials). Colours are as in **a**. **d**, The same as in **c**, but for a neuron activated by right-relative-to-head contacts on L2 and L4 (head centric). **e**, Still frames showing examples of the tongue-contact and head-contact angle (left). Colours are as in Fig. 1b. Middle, the percentage of L2- and L4-modulated neurons correlated with contact angle in a tongue-centric frame (gold), head-centric frame (red), both (pink) or neither (grey). Right, R^2 values from each neuron's correlation between firing rate after L4 contact and contact angles computed in tongue-centric (x-axis) or head-centric (y-axis) frames. The circled conjunctive neuron corresponds to Extended Data Fig. 8g. Statistical analysis was performed using two-sided hierarchical bootstrap tests. Exact statistical values are provided in Supplementary Tables 12 and 13. Panels **b–d** were adapted from ref. 8, Springer Nature Limited. Scale bar, 1 mm (**e**).

($n = 93$ out of 359 neurons, $n = 4$ mice). We next compared L2 and L4 nick-site selectivities for each neuron and found that some exhibited tongue-position-independent nick-site selectivity. For example, the neuron in Fig. 4c increased its firing rate after right surface nicks on both L2 and L4, even though the tongue was at distinct positions at the moments of contact. Yet the nick responses in other neurons depended on tongue position. For example, the neuron in Fig. 4d was activated by contacts on both L2 and L4 that specified a spout to the right of the head, but was not activated by right nicks on L4 that indicated a centred spout.

To quantify the contributions of both head- and tongue-based coordinate frames to each neuron's response profile, we correlated each neuron's L4 tactile response to the contact angle encoded in tongue-centred

(relative to the tongue midline) or head-centred (relative to the head midline) coordinates (Fig. 4e). The neural responses of some neurons were strongly anchored in a tongue-based reference frame, others in a head-based frame and yet others exhibited conjunctive tuning to both tongue- and head-based coordinate systems (Extended Data Fig. 8g). Notably, circuits that implement coordinate transformations in other systems also exhibit neuronal representations anchored in both single and conjunctive reference frames^{33–36}.

We next reasoned that the process of transforming tactile signals from a tongue-to-head based reference frame may impose a delay. We hypothesized that neurons with tongue-centred tactile responses might have lower contact latencies than neurons with head-centred responses, as head-centred neurons need to additionally weigh

information about tongue position. Indeed, we found that neurons with a head-based reference frame had significantly longer contact latencies (Extended Data Fig. 8h), similar to previous research examining analogous ego-to-allocentric sensorimotor transformations in the *Drosophila* central complex³⁷.

Implementation of a tongue-to-head-based coordinate transformation for tactile representations requires information about the position of the tongue, which could arise as a result of premotor signals, proprioceptive feedback and/or efference copy. One indicator of tongue position is phase in the lick cycle, which we quantified using the volume of the tongue visible outside the mouth (Extended Data Fig. 9a–d and Methods). latSC neuronal activity strongly co-varied with lick phase (Extended Data Fig. 9a–c), as previously reported^{21,22}, and neurons were locked to lick phase with a wide range of lags (Extended Data Fig. 9d). Yet, to implement lateralized touch-guided corrections in our task, the latSC additionally needs detailed information about tongue position in the mediolateral plane, which is unspecified by lick phase alone. We used generalized linear models (GLMs) to test whether fine details of 3D tongue position were encoded in the activity of individual latSC neurons in a brief interval preceding L4 contact (Extended Data Fig. 9e,f and Methods; 50 ms before L4 protrusion to L4 contact). Notably, L4 tongue position was strongly encoded in many latSC neurons before L4 contact (Extended Data Fig. 9g–i), and the mediolateral position of the tongue tip provided the strongest contribution to latSC spiking immediately before L4 contact on average (Extended Data Fig. 9h,i). Together, these analyses show that the latSC has the necessary information with the appropriate timing for implementing a tongue- to head-based coordinate transformation that may be important for using the sense of touch to localize the spout in space, which in turn is important for aiming the next lick.

A topographic map for tongue aiming

To test whether the latSC can have a causal role in lick generation and aiming, we optogenetically microstimulated four different regions spanning 800 μm along the anterior–posterior (AP) axis of each latSC hemisphere for 400 ms (Fig. 5a,c (top), Extended Data Fig. 10a–c and Methods). Photostimulation of the latSC at each site reliably and rapidly elicited tongue protrusions and lick bouts even when photostimulation occurred outside of any task structure (Fig. 5b,e,f and Extended Data Fig. 10f–m). Critically, the precise photostimulation site was significantly correlated with the protrusion angle of the first stimulation-evoked lick (Fig. 5c,d, Extended Data Fig. 10d,e, Supplementary Video 8 and Methods). Posterior stimulation sites directed the tongue more laterally and anterior sites more medially on the contralateral side (Fig. 5c,d and Extended Data Fig. 10d,e). A similar topographic layout for saccades and visually guided orienting is observed in the SC across many species^{13–15,30}. Together with our electrophysiological data (Fig. 3c), these findings show that the latSC contains a mechanosensorimotor map for touch-guided tongue control with a similar topography to visuomotor maps for saccades and orienting^{13,14}.

Discussion

Humans rely on the sense of touch to guide tongue movements during eating, drinking and vocalizing^{3,38}. We found that mice also use precise tactile feedback while drinking water from a spout. Importantly, when mice nickered a spout with the left part of their tongue surface on a straight lick, they accurately re-aimed the next lick to a left spout position. But the same nick on a right-aimed lick caused accurate re-aiming to a centred spout. Position-dependent reactions to sensory feedback require sensorimotor coordinate transformations that map postural information onto a coordinate system relevant for aiming movement. In primates, sensorimotor cortical pathways mediate touch- and visually guided reaching and grasping^{1,39}, and the SC has been implicated

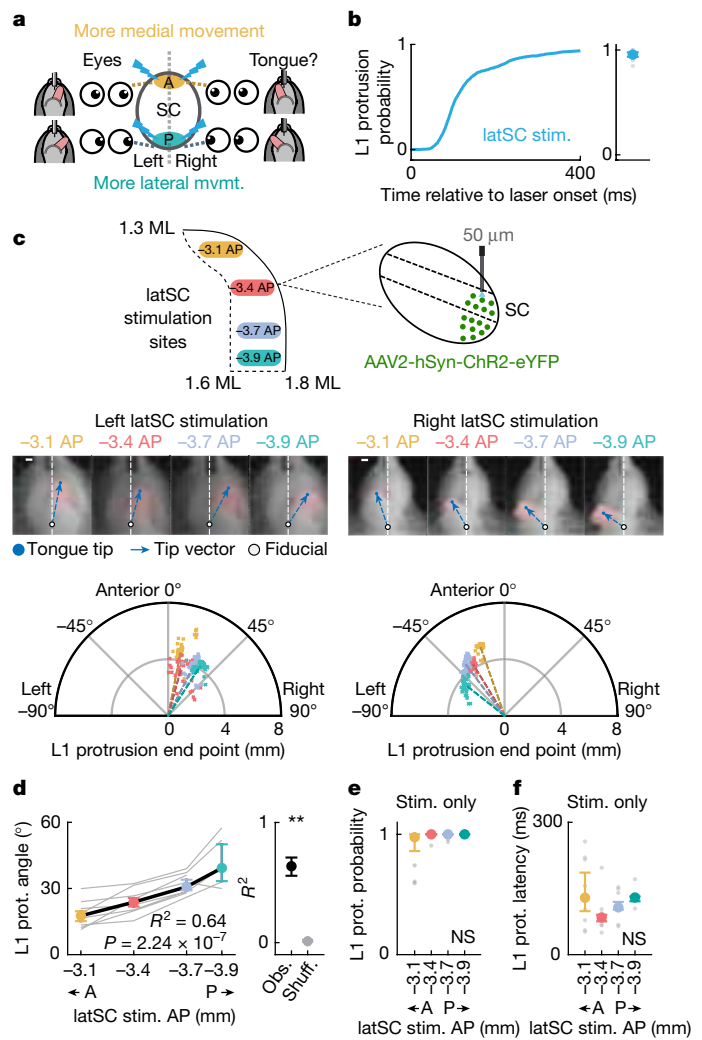


Fig. 5 | latSC photostimulation reveals a topographic map for tongue aiming.

a, Hypothesis schematic. In many species, stimulation of posterior (P) sites in the SC evoke more lateralized shifts in contralateral gaze than anterior (A) sites. Multisite photostimulation in the latSC tested for similar functional tongue control. **b**, Cumulative probability of L1 protrusion for latSC photostimulation (stim.) trials (cyan) (left). Right, L1 protrusion probability. $n = 6$ mice. **c**, Photostimulation example data. Top, experimental schematic. Photoactivation was targeted to four sites spanning 800 μm along the AP axis of the latSC (left). Middle, still frames from an example left and right latSC photoactivation trial for each AP target at protrusion offset. The tongue tip (dot) and the tip vector (dashed line) are shown in blue, and the fiducial point is shown as a white dot. Bottom, polar plots of L1 protrusion end points for an example left and right latSC photostimulation session. The individual coloured points represent individual trials, and the coloured dashed lines indicate the median for each AP target. Note that the L1 protrusion end point depended on the stimulation site. AP and ML values are in mm. **d**, **e**, **f**, latSC-photostimulation-evoked L1 protrusion angles are correlated with the latSC photostimulation site ($n = 8$ mice, left). The grey lines represent individual mice. Right, the R^2 for the observed (obs.) correlation between photostimulation site and L1 protrusion angle (black) compared with shuffled (shuff.) data (grey). **e**, **f**, The L1 protrusion probability (e) and latency (f) did not differ between latSC stimulation sites. Data in c–f are colour coded by stimulation site in the latSC. The colours in c–f correspond to latSC implant sites as shown in c. Coloured data in d–f are median \pm IQR. Statistical analysis was performed using two-sided shuffle tests (d) and Kruskal–Wallis tests (e and f). Exact statistical values are provided in Supplementary Table 14. Panel a was adapted from ref. 8, Springer Nature Limited. Scale bars, 1 mm (c).

in visual-, auditory- and somatosensory-guided orienting^{14,35,40,41}. Yet spinalized frogs and *Drosophila* exhibit body-position-dependent responses to stimuli^{34,42}, showing that diverse circuit architectures

can implement coordinate transformations that are important for sensory-feedback-based aiming.

Touch-guided lick aiming did not require activity in cortical areas previously associated with licking^{11,12} and instead required activity in the latSC^{21,22}. Notably, several aspects of SC function canonically associated with other types of stimulus-guided orienting were recapitulated in our experiments. First, unilateral latSC inactivations selectively impaired contralateral touch-guided re-aiming, much like unilateral SC inactivations reduce orienting to contralateral visual targets^{24,25}. Second, viral tracing identified a lingual region of the trigeminal nucleus that projected directly to the latSC, revealing an early sensory input analogous to direct retinal inputs to SC¹³. Third, latSC neurons exhibited receptive fields for mostly contralateral touch sites, and could represent these tactile events in the tongue, head and conjunctive reference frames. Fourth, latSC neural activity also encoded information about tongue position and the aiming of upcoming licks, which could arise from premotor or efference copy signals, or proprioceptive feedback. Thus, the latSC exhibits a combination of signals that may be important for implementing coordinate transformations necessary for sensorimotor feedback control^{33,35,39,43}. Finally, latSC photomicrostimulation evoked licks and aimed them in accordance with a topographic map similar to that known to be used for saccades and orienting, in which more posterior stimulation sites evoke more contralaterally aimed movements^{13–15,30,44}. Together, these data show that the latSC contains a mechanosensorimotor map for touch-guided tongue control that shares mechanistic features observed in visually guided orienting^{17,18}. With recent advances examining tongue kinematics in marmosets and macaques, it will be possible to test whether the primate SC also implements touch-guided control⁴⁵.

A comparative approach across species, behaviours and effectors can distinguish general principles from specialized solutions to narrower control problems. The mammalian SC and analogous tectal regions in other species use sensorimotor maps to direct stimulus-guided orienting across a range of species-specific sensory modalities^{13,14,30,44,46,47}, including whisking in rodents^{18,31,32}, echolocation in bats⁴⁸, binocular vision in raptors⁴⁹ and infrared vision in snakes⁵⁰. The topographic architecture of the SC/optic tectum is thought to implement a winner-take-all decision process important for selecting a single direction for orienting and escape⁴⁶. Touch-guided tongue control may be similarly dependent on the SC because, like orienting, it could require a rapid selection process for both a salient sensory event and an ensuing motor response. Notably, we observed a diversity of neural signals in the latSC, including tactile responses in multiple coordinate frames that may be important for touch-guided control, as well as orienting or reaching towards food or water sources. Finally, the latSC has multiple layers, cell types and complex connectivity with brainstem, cerebellar and forebrain structures, and our findings do not rule out the possibility that other circuits may also participate in tactile–motor coordinate transformations that are important for tongue control. Future studies can leverage touch-guided tongue control in head-fixed mice to further clarify microcircuit-level mechanisms of coordinate transformations that are important for sensory-guided action^{33,34}.

Online content

Any methods, additional references, Nature Portfolio reporting summaries, source data, extended data, supplementary information, acknowledgements, peer review information; details of author contributions and competing interests; and statements of data and code availability are available at <https://doi.org/10.1038/s41586-024-08339-3>.

- Kleinfeld, D. & Deschênes, M. Neuronal basis for object location in the vibrissa scanning sensorimotor system. *Neuron* **72**, 455–468 (2011).
- Bensmaia, S. & Helms Tillery, S. I. In *The Human Hand as an Inspiration for Robot Hand Development* (eds Balasubramanian, R. & Santos, V. J.) 143–157 (Springer, 2014).

- Laurence-Chasen, J. D., Arce-McShane, F. I., Hatsopoulos, N. G. & Ross, C. F. Loss of oral sensation impairs feeding performance and consistency of tongue-jaw coordination. *J. Oral Rehabil.* **49**, 806–816 (2022).
- Donohue, C. et al. Profiles of dysarthria and dysphagia in individuals with amyotrophic lateral sclerosis. *J. Speech Lang. Hear. Res.* **66**, 154–162 (2023).
- Rabin, E. & Gordon, A. M. Tactile feedback contributes to consistency of finger movements during typing. *Exp. Brain Res.* **155**, 362–369 (2004).
- Johansson, R. S., Hger, C. & Bäckström, L. Somatosensory control of precision grip during unpredictable pulling loads. III. Impairments during digital anesthesia. *Exp. Brain Res.* **89**, 204–213 (1992).
- Moore, J. D., Kleinfeld, D. & Wang, F. How the brainstem controls orofacial behaviors comprised of rhythmic actions. *Trends Neurosci.* **37**, 370–380 (2014).
- Bolu, T. et al. Cortex-dependent corrections as the tongue reaches for and misses targets. *Nature* **594**, 82–87 (2021).
- Binkofski, F., Kunesch, E., Classen, J., Seitz, R. J. & Freund, H. J. Tactile apraxia: unimodal apraxic disorder of tactile object exploration associated with parietal lobe lesions. *Brain* **124**, 132–144 (2001).
- Pruszyński, J. A., Johansson, R. S. & Flanagan, J. R. A rapid tactile-motor reflex automatically guides reaching toward handheld objects. *Curr. Biol.* **26**, 788–792 (2016).
- Xu, D. et al. Cortical processing of flexible and context-dependent sensorimotor sequences. *Nature* **603**, 464–469 (2022).
- Mayrhofer, J. M. et al. Distinct contributions of whisker sensory cortex and tongue-jaw motor cortex in a goal-directed sensorimotor transformation. *Neuron* **103**, 1034–1043 (2019).
- Sparks, D. L. Neural cartography: sensory and motor maps in the superior colliculus. *Brain Behav. Evol.* **31**, 49–56 (1988).
- Allen, K. M., Lawlor, J., Salles, A. & Moss, C. F. Orienting our view of the superior colliculus: specializations and general functions. *Curr. Opin. Neurobiol.* **71**, 119–126 (2021).
- Zahler, S. H. et al. Hindbrain modules differentially transform activity of single collicular neurons to coordinate movements. *Cell* **186**, 3062–3078 (2023).
- Wolf, A. B. et al. An integrative role for the superior colliculus in selecting targets for movements. *J. Neurophysiol.* **114**, 2118–2131 (2015).
- Basso, M. A. & May, P. J. Circuits for action and cognition: a view from the superior colliculus. *Annu. Rev. Vis. Sci.* **3**, 197–226 (2017).
- Dräger, U. C. & Hubel, D. H. Topography of visual and somatosensory projections to mouse superior colliculus. *J. Neurophysiol.* **39**, 91–101 (1976).
- Schiller, P. H. & Stryker, M. Single-unit recording and stimulation in superior colliculus of the alert rhesus monkey. *J. Neurophysiol.* **35**, 915–924 (1972).
- Robinson, D. A. Eye movements evoked by collicular stimulation in the alert monkey. *Vision Res.* **12**, 1795–1808 (1972).
- Rossi, M. A. et al. A GABAergic nigrothalamic pathway for coordination of drinking behavior. *Nat. Neurosci.* **19**, 742–748 (2016).
- Lee, J. & Sabatini, B. L. Striatal indirect pathway mediates exploration via collicular competition. *Nature* **599**, 645–649 (2021).
- Li, N., Chen, T. W., Guo, Z. V., Gerfen, C. R. & Svoboda, K. A motor cortex circuit for motor planning and movement. *Nature* **519**, 51–56 (2015).
- Hikosaka, O. & Wurtz, R. H. Modification of saccadic eye movements by GABA-related substances. I. Effect of muscimol and bicuculline in monkey superior colliculus. *J. Neurophysiol.* **53**, 266–291 (1985).
- Schiller, P. H., Sandell, J. H. & Maunsell, J. H. The effect of frontal eye field and superior colliculus lesions on saccadic latencies in the rhesus monkey. *J. Neurophysiol.* **57**, 1033–1049 (1987).
- Greenwood, L. F. & Sessle, B. J. Inputs to trigeminal brain stem neurones from facial, oral, tooth pulp and pharyngolaryngeal tissues: II. Role of trigeminal nucleus caudalis in modulating responses to innocuous and noxious stimuli. *Brain Res.* **117**, 227–238 (1976).
- Borke, R. C., Nau, M. E. & Ringel, R. L. Jr. Brain stem afferents of hypoglossal neurons in the rat. *Brain Res.* **269**, 47–55 (1983).
- Benavidez, N. L. et al. Organization of the inputs and outputs of the mouse superior colliculus. *Nat. Commun.* **12**, 4004 (2021).
- Huerta, M. F., Frankfurter, A. & Harting, J. K. Studies of the principal sensory and spinal trigeminal nuclei of the rat: projections to the superior colliculus, inferior olive, and cerebellum. *J. Comp. Neurol.* **220**, 147–167 (1983).
- Gandhi, N. J. & Katnani, H. A. Motor functions of the superior colliculus. *Annu. Rev. Neurosci.* **34**, 205–231 (2011).
- Wang, L., Sarnaik, R., Rangarajan, K., Liu, X. & Gang, J. Visual receptive field properties of neurons in the superficial superior colliculus of the mouse. *J. Neurosci.* **30**, 16573–16584 (2010).
- Lee, K. H., Tran, A., Turan, Z. & Meister, M. The sifting of visual information in the superior colliculus. *eLife* **9**, e50678 (2020).
- Salinas, E. & Abbott, L. F. Transfer of coded information from sensory to motor networks. *J. Neurosci.* **15**, 6461–6474 (1995).
- Mussells Pires, P., Zhang, L., Parache, V., Abbott, L. F. & Maimon, G. Converting an allocentric goal into an egocentric steering signal. *Nature* **626**, 808–818 (2024).
- Groh, J. M. & Sparks, D. L. Two models for transforming auditory signals from head-centered to eye-centered coordinates. *Biol. Cybern.* **67**, 291–302 (1992).
- Jay, M. F. & Sparks, D. L. Sensorimotor integration in the primate superior colliculus. II. Coordinates of auditory signals. *J. Neurophysiol.* **57**, 35–55 (1987).
- Lyu, C., Abbott, L. F. & Maimon, G. Building an allocentric travelling direction signal via vector computation. *Nature* **601**, 92–97 (2022).
- Parrell, B. & Houde, J. Modeling the role of sensory feedback in speech motor control and learning. *J. Speech Lang. Hear. Res.* **62**, 2963–2985 (2019).
- Andersen, R. A. & Zipser, D. The role of the posterior parietal cortex in coordinate transformations for visual-motor integration. *Can. J. Physiol. Pharmacol.* **66**, 488–501 (1988).
- Groh, J. M. & Sparks, D. L. Saccades to somatosensory targets. III. Eye-position-dependent somatosensory activity in primate superior colliculus. *J. Neurophysiol.* **75**, 439–453 (1996).
- Jay, M. F. & Sparks, D. L. Auditory receptive fields in primate superior colliculus shift with changes in eye position. *Nature* **309**, 345–347 (1984).

42. Fukson, O. I., Berkinblit, M. B. & Feldman, A. G. The spinal frog takes into account the scheme of its body during the wiping reflex. *Science* **209**, 1261–1263 (1980).
43. Kakei, S., Hoffman, D. S. & Strick, P. L. Sensorimotor transformations in cortical motor areas. *Neurosci. Res.* **46**, 1–10 (2003).
44. Helmbrecht, T. O., Dal Maschio, M., Donovan, J. C., Koutsouli, S. & Baier, H. Topography of a visuomotor transformation. *Neuron* **100**, 1429–1445 (2018).
45. Laurence-Chasen, J. D., Ross, C. F., Arce-McShane, F. I. & Hatsopoulos, N. G. Robust cortical encoding of 3D tongue shape during feeding in macaques. *Nat. Commun.* **14**, 2991 (2023).
46. Mysore, S. P. & Knudsen, E. I. The role of a midbrain network in competitive stimulus selection. *Curr. Opin. Neurobiol.* **21**, 653–660 (2011).
47. Nagy, A., Kruse, W., Rottmann, S., Dannenberg, S. & Hoffmann, K.-P. Somatosensory-motor neuronal activity in the superior colliculus of the primate. *Neuron* **52**, 525–534 (2006).
48. Valentine, D. E. & Moss, C. F. Spatially selective auditory responses in the superior colliculus of the echolocating bat. *J. Neurosci.* **17**, 1720–1733 (1997).
49. Frost, B. J., Wise, L. Z., Morgan, B. & Bird, D. Retinotopic representation of the binocular eye of the kestrel (*Falco sparverius*) on the optic tectum. *Vis. Neurosci.* **5**, 231–239 (1990).
50. Hartline, P. H., Kass, L. & Loop, M. S. Merging of modalities in the optic tectum: infrared and visual integration in rattlesnakes. *Science* **199**, 1225–1229 (1978).

Publisher's note Springer Nature remains neutral with regard to jurisdictional claims in published maps and institutional affiliations.

Springer Nature or its licensor (e.g. a society or other partner) holds exclusive rights to this article under a publishing agreement with the author(s) or other rightsholder(s); author self-archiving of the accepted manuscript version of this article is solely governed by the terms of such publishing agreement and applicable law.

© The Author(s), under exclusive licence to Springer Nature Limited 2025

Article

Methods

Animals and surgery

Male and female mice aged 10–24 weeks old were used in this study (21 VGAT-ChR2-eYFP mice, JAX, 014548; 6 *Slc32a1^{tm2(cre)Low/Mwaj}* (*Vgat-Ires-cre*) mice, JAX, 028862; 16 C57BL/6J mice, JAX, 000664; and 3 *Rosa^{26LSL-tdTomato}* (Ai14) mice, JAX, 007914). Mice were individually housed under a 12 h–12 h light–dark cycle (ambient temperature, 72 °F; relative humidity, 50%) and all of the experiments were performed during the dark cycle. Sample sizes for each experiment were chosen to be within ethical constraints and similar to those used within the field. Mice were allocated randomly to experimental conditions and no blinding was performed. All of the procedures were in accordance with NIH guidelines and approved by the Cornell Institutional Animal Care and Use Committee, an AAALAC-accredited institution.

Before surgeries, mice were anaesthetized with 5% isoflurane. Fur covering the scalp was trimmed, and mice were then head-fixed in a stereotaxic apparatus (Kopf Instruments and Leica Biosystems). An electric heat pad was used to maintain the mouse body temperature and isoflurane concentration was kept between 1 and 2% throughout surgeries. Mice were administered buprenorphine (0.05 mg per kg, SQ) for pain management and ocular ointment was applied to protect the eyes. The scalp was then cleaned with betadine and 70% alcohol and an incision was made along the midline to expose the skull. Enrofloxacin (5 mg per kg, SQ) and carprofen (5 mg per kg, SQ) were administered post-operatively. AP and mediolateral (ML) stereotaxic coordinates below were taken relative to bregma, and dorsoventral (DV) was taken from the skull surface.

For optogenetic inhibition of cortical regions, craniotomies were made over the ALM (2.5 mm AP, ±1.5 mm ML), TJM1 (1.8 mm AP, ±2.6 mm ML) or TJS1 (0.3 mm AP, ±3.5 mm ML)¹² in VGAT-ChR2-eYFP mice. We implanted two 400 μm optic fibres (0.39 NA, Thorlabs) bilaterally over these areas and covered the exposed brain surface with silicone gel (Kwik-Cast, World Precision Instruments). Optic fibres were implanted with a 24 (30) degree lateral tilt in the ML/DV plane for TJM1 (TJS1). Cannulas were cemented to the skull with Metabond (Parkell). A custom-modified RIVETS headplate was then implanted over the skull⁵¹. We calibrated our cortical inactivations in the ALM in previously published work using the same setups and laser powers used for these inactivations⁸.

For optogenetic inhibition of the SC through the SNr–SC pathway, 400 nl of AAV5-Ef1α^{n/n}-hChR2(H134R)-eYFP (Addgene) was bilaterally injected into the SNr (−3.2 mm AP, ±1.5 mm ML, −4.3 mm DV) of *Vgat-Ires-cre* mice, and two 100 μm optic fibres (0.22 NA, Doric Lenses) were implanted bilaterally over the intermediate layers of the SC (−3.4 mm AP, ±1.5 mm ML, −2.0 mm DV) along with a headplate. We waited at least 4 weeks for viral expression before performing any manipulations, during which time mice underwent behavioural training. For optogenetic inhibition of SC in VGAT-ChR2-eYFP mice, we implanted two 100 μm optic fibres bilaterally.

For photostimulation of the SC, 500 nl of AAV2/hSyn-hChR2(H134R)-eYFP-WPRE-PA or AAV5/hSyn-hChR2(H134R) (UNC Vector Core, a gift from K. Deisseroth) was unilaterally injected into SC (−3.4 mm AP, ±1.5 mm ML, −2.6 mm DV) of C57BL6/J mice. Four fiducials were made with marker ink around the craniotomy for later calibration. The craniotomy was then sealed with silicone gel, and a headplate was implanted with a thin layer of clear Metabond covering the skull surface.

For acute electrophysiology experiments, fiducials were made bilaterally over ALM and/or SC, as well as visual cortex (−2.3 mm AP, ±3.0 mm ML), and marked with black ink. Additional fiducials over bregma and lambda were also made for later calibration. A headplate was then implanted with a thin layer of clear Metabond covering the skull surface.

For cortical lesions, fiducials were marked bilaterally over ALM, TJM1 and TJS1, with additional four fiducials for calibrating skull levelling later. A headplate was then implanted with a thin layer of clear

Metabond covering the skull surface. After mice were trained in the behavioural task and pre-lesion data were collected, the clear Metabond covering the cortical areas was removed and resealed with silicone gel. About 24 h later, 125 nl of 4% N-methyl-D-aspartic acid (Sigma-Aldrich, M3262, diluted in 1× DPBS (Corning) with 1 M NaOH) was injected into each site in the ALM (1.0 mm and 0.6 mm below the brain surface), TJM1 (1.0 mm and 0.6 mm below the brain surface) and TJS1 (0.32 mm AP, ±3.45 mm ML, 0.6 mm below the brain surface; 0.32 mm AP, ±3.10 mm ML, 1.0 mm below the brain surface). We decided to perform the surgeries on two separate days to ensure the survival of animals by reducing the length of anaesthesia on a single day. Moreover, supplementary water and Nutra-Gel (Bio-serv) was given to animals from 1 day before the surgeries to 1–3 days after, depending on the recovery status indicated by weight.

Viral tracing

A total of 2–3 μl of AAV1-hSyn-Cre was injected into the tongues of Ai14 reporter mice to label processes of primary trigeminal afferents that innervate the tongue. Moreover, 100 nl of AAV5-CAG-GFP was injected dorsally into SpVO to label secondary trigeminal neurons. Mice were euthanized after around 8–12 weeks. AAV1-hSyn-Cre was a gift from J. M. Wilson (Addgene, 105553-AAV1). AAV5-CAG-GFP was a gift from E. Boyden (Addgene, 37825-AAV5).

Histology

Mice were euthanized with a lethal dose of intraperitoneal sodium pentobarbital, followed by pericardial perfusion with 4% paraformaldehyde (Electron Microscopy Services) in 1× PBS (Corning). Brains were extracted, sliced to 50 or 100 μm thickness with a Leica VT1000 S vibratome, mounted onto glass slides with PVA-DABCO (Sigma Aldrich) and then imaged under the Zeiss LSM 710 confocal microscope. To validate cortical lesions, brain slices were first incubated in 0.6% Triton X-100 in 1× PBS for 20 min, washed in 1× PBS (three times for 5 min), stained with mouse anti-NeuN antibody conjugated with Alexa Fluor 555 (EMD Millipore, MAB377A5, 1:250 dilution in 1× PBS with 0.3% Triton X-100) for 1.5 h and finally washed again in 1× PBS (three times for 5 min).

Behaviour

The behavioural setup was as previously described⁸. In brief, the tongue was captured from side and bottom views by placing a mirror (Thorlabs, ME1S-P011') at 45° underneath the face of the mouse. Videos were acquired at 1,000 fps with a Phantom VEO 410L camera and a Nikon 105 mm f/2.8D AF Micro-Nikkor lens. An 880-nm-wavelength IR strobe (AOS Technologies, manufacturing discontinued) or 850-nm-wavelength infrared ring light (Smart Vision Lights) was used to provide illumination of the tongue during video imaging. To build the behavioural rig, we 3D-printed custom-made head clamps for fixation. 1 kHz audio cues were played through tone generators (Med Associates), and a blue LED (Amazon) optogenetic masking light was delivered throughout the entire trial period. Water was dispensed through a 0.072 inch outer-diameter stainless steel spout (Small Parts) using a 24 V or 5 V solenoid valve (The Lee Company). Spout contacts were detected either with a capacitive touch sensor (Atmel), or a custom-made electrical lick sensor⁵² to increase contact detection sensitivity and reduce contact-induced noise in electrophysiology recordings. For double-step experiments, water spouts were attached to two orthogonally arranged linear motors (Faulhaber) mounted on guide rails (McMaster-Carr). Control signals sent to the controllers for the servo motors (Faulhaber) were recorded throughout the experiment, enabling us to track the spout during behavioural sessions (see the ‘Tongue contact location tracking’ section). During experiments, water spouts were displaced by a precalibrated distance along both AP and ML axes. Custom LabVIEW codes for behavioural tasks were run using NI sbRIO-9636 or -9637 field-programmable gate array (FPGA)-based acquisition systems.

Behavioural paradigms and training

Water deprivation started 5 days after surgery. Mice under water deprivation received at least 1 ml of water daily from performing behavioural tasks. Supplementary water was provided to meet this requirement if the mice did not collect enough water from tasks, or on days on which the mice did not take part in any behavioural testing. After the body weight of the mice stabilized (typically around 80% of the original weight), mice began behavioural training following a similar procedure to that previously described⁸. Mice were first habituated to head fixation on the behavioural rig for 3 days. The mice then began cued-lick training in a trial structure. To encourage mice to lick the water spout, water was dispensed at the cue onset on the first few sessions. Once mice reliably began to associate the auditory cue with a water reward (typically, after one to three sessions), we made the water dispense contingent on the first spout contact within 1.3 s of the auditory cue. We then imposed a 1 s no-spout-contact window before the audio cue to discourage premature licking before cue onset. Any spout contact during this window ended the trial and initiated a new intertrial interval. The intertrial interval was randomly chosen from an exponential distribution with a flat hazard rate. Once mice could reliably trigger water dispense for over 95% of trials in a session with very few licks during the inter-trial interval and less than 10% no-spout-contact window violations, we either started the photomicrostimulation experiment or moved on to the next phase of training for the left/right doublestep paradigm.

For all analyses, with the exception of photostimulation experiments, lick numbers (L1, L2 and so on) are defined relative to the first lick that made contact with the spout after the auditory cue on a given trial. For photostimulation experiments, lick numbers were defined relative to stimulation onset. For assessing the kinematic impairments in cortical lesioned mice (Extended Data Fig. 4), the first lick was defined as the first lick after auditory cue onset regardless of spout contact.

For left/right displacement experiments, the water spout was subtly (-1.1 mm) displaced to the left or right at L1 contact offset (left, centre, right positions each with 33% probability). For left or right positions the spout was also moved slightly closer in the AP direction such that the radial distance from the jaw to the spout was similar across all possible spout positions. Except for the recentring experiment described below, the spout remained at the same position for the remainder of the trial after the displacement and only moved back to the centre position 1 s before the start of the next trial. To ensure that the mice could not detect spout movements by seeing, whisking or hearing spout movements, we placed the water spout ~3 mm beneath the snout out of the visual field and trimmed the whiskers and orofacial hair of mice every 2–4 days in all experiments. The auditory cue, which plays throughout the duration of the trial, served as a masking sound for any residual noise made by the servo motors, which were already quiet. Water was dispensed on L2 contact or L3 contact (Extended Data Fig. 1). Mice were trained with this new task setup for 7–14 days, with most mice already exhibiting at least some L3 re-aiming on day 1 (data not shown). For the first few days of training, we allowed only two consecutive spout displacements to the same direction to ensure that mice did not develop a directional licking bias on L2. This limit was increased to ten during experiments.

For recentring experiments, water spouts were randomly (~35% probability) moved back to the centre position at L3 contact offset. For 3 out of 5 mice, the recentred position was slightly (~0.5 mm) closer than the initial centre position to ensure that mice would still nick the spout with lateral tongue protrusions on L4. Recentring trials first began 1–3 days before experiments to familiarize the mice with the task. During training, we lowered the probability of recentring to only 15–20% to prevent mice from potentially developing a centre protrusion bias on L4.

For cortical lesion experiments, two out of five animals exhibited such pronounced hypometria that they were unable to reach the 3 mm spout distance used in other experiments. We anticipated this and collected pre-lesion data at various spout distances, including

approximately 2.25 mm, which all animals were able to reach 6–16 days after lesion. Data from all mice in Extended Data Fig. 4 were collected at this 2.25 mm distance.

Optogenetic inactivation

We used laser diode light sources (LDFLS_450-450, Doric Lenses), attached to an optical rotary joint splitter (FRJ_1x2i_FC-2FC_0.22, Doric Lenses) and delivered light bilaterally or unilaterally to the implanted optic fibres using 200 µm, 0.22 NA or 400 µm, 0.43 NA, lightly armoured metal-jacket patch cords (Doric Lenses). The light sources were set to analogue input mode and driven with a square pulse for 250 ms with a 50 ms ramp down starting at L2 contact onset, which was detected in real time. For cortical photoinactivations, laser power was set to 10 mW. For bilateral SC photoinactivation, the laser power was set to 5 mW. For unilateral SC photoinactivation, most mice were inactivated with 5 mW. However, one mouse was inactivated with 1 mW power. We observed no difference in the magnitude of the effect of unilateral manipulations between the 1 and 5 mW cohorts (data not shown), and we therefore combined the data. Pulse duration and laser powers were identical for photovalue experiments.

Optogenetic stimulation

Light was delivered at 1 mW with laser diode light sources through a 200 µm, 0.22 NA lightly armoured metal-jacket patch cord (Doric Lenses) to a very thin silica optic fibre (50 µm diameter, 0.22 NA, Doric Lenses). Simulations performed by Doric Lenses with a scattering model for the same optic fibre parameters predicted that this would illuminate a volume underneath the fibre constrained approximately within 50–70 µm in the AP and ML direction and extending at least 250 µm in the DV direction (incident flux around 100 mW mm⁻² at 250 µm underneath the tip). At 12–24 h before the start of experiments, the thin layer of Metabond covering the craniotomy was removed and resealed with a layer of silicone gel. During the experiment, the optic fibre was held in place with a custom-made fibre cannula holder and targeted stereotactically to different sites of the latSC (-3.1 to -3.9 mm AP, ±1.3–1.6 mm ML for -3.1 mm AP and ±1.6–1.8 mm ML for all other sites). The DV coordinate for each site was adjusted between -1.75 to -2.45 mm for each site such that the fibre tip sat above the intermediate layer of SC. AP and ML coordinates were calibrated based on previously marked fiducials centred at bregma and lambda, and DV coordinates were based on micromanipulator readings relative to the bregma skull surface. After acute fibre implantation, the craniotomy was filled with silicone gel to reduce brain movement and 1× PBS was pipetted into the headplate to prevent the brain from drying. For each site, laser light was first delivered at cue onset for 250–400 ms (adjusted to ensure that the laser was on for at least the entire duration of L1) with ~45% probability for about 120 trials, then for around 30 trials without auditory cue to indicate trial structures. One to three sites were tested with this sequence on each day, after which the craniotomy was refilled with silicone gel. On the last day of the experiment, thin needles (NF36BV WPI) were coated with a lipophilic dye (DiI or DiD, Thermo Fisher Scientific) to mark all previously stimulated sites.

Acute electrophysiology

Extracellular recordings were made acutely using 64-channel silicon probes (ASSY-77H6, Cambridge Neurotech). For latSC photovalue experiments, a 200 µm optic fibre was attached to the silicon probe (ASSY-77H6 with 200 µm fibre, Cambridge Neurotech). The 64-channel voltage signals were amplified, filtered and digitized (16 bit) on a headstage (Intan Technologies), recorded on a 512-channel Intan RHD2000 recording controller (sampled at 20 kHz) and stored for offline analysis. At 12–24 h before recording, a small (1.5 mm diameter) craniotomy was made unilaterally over the SC, as well as the visual cortex. A ground screw with a soldered gold pin (A-M systems) was implanted into the skull overlying the visual cortex away from the recording site and held

Article

in place with Metabond. The probes were targeted stereotactically to the SC, lowered to a depth of 2.1–2.6 mm below the dura surface. Recording sites in the AP plane spanned 1 mm from −2.9 to −3.9 mm AP. The ML recording location was targeted to the lateral region of the SC at each AP site, which changed with the contour of the SC along the AP axis from −1.2 mm ML at more anterior sites to −1.6 mm ML at more posterior sites. For cortical photovalidation experiments, probes were targeted to the deep (−0.8 to −1.2 mm DV) or superficial (−0.3 to −0.8 mm DV) layers of the ALM (−2.5 mm AP, ±1.5 mm ML) and a 400 μm optic fibre was placed on the dura surface. Photovalidation recordings were performed only in the ALM as photoinactivation methods were identical for all three cortical regions investigated (ALM, TJM1 and TJS1). AP and ML coordinates were calibrated based on the fiducials previously marked and DV coordinates were based on micromanipulator readings. After probe insertion, 2% low-melting-point agarose (A9793-50G, Sigma-Aldrich) in 1× PBS was pipetted in the craniotomy to reduce brain movement and additional PBS was pipetted into the headplate to prevent the brain from drying. Three to seven recordings were made from each craniotomy. At the end of each session, the craniotomy was covered with silicone gel. Probes were coated with a lipophilic dye (Dil or DiD, Thermo Fisher Scientific) before each recording to ensure placement in the region of interest.

Lingual segmentation and kinematics analysis

Lingual segmentation. We implemented a semantic segmentation convolutional neural network (U-NET) to identify and segment the tongues from high-speed videography as previously described⁸. Our network was trained on 7,681 frames randomly selected from 36 mice. Training data for tongue segmentation were hand-traced using a custom MATLAB GUI. We trained networks for side and bottom views in batches of 256 images, using the ‘adam’ optimizer and a binary cross entropy loss function. The networks were trained until the loss function reached an asymptotic value of 0.0035 for the side-view network and 0.0036 for the bottom-view network, with a validation accuracy of 0.9984 and 0.9985, respectively. Both networks reached asymptotic performance within 5,000 epochs.

Lingual kinematics analysis. The full 3D kinematics of the tongue tip from high-speed videography were obtained as previously described⁸. In brief, we performed a visual hull reconstruction from the side and bottom view silhouettes of the tongue. The centroid of the tongue was identified from the 3D voxels and a two-step search process was implemented to locate the tongue tip. Tongue tip kinematics were smoothed using an 8-pole, 50 Hz low-pass filter. Lick phases were defined based on the rate of volume changes calculated from the 3D tongue reconstruction as follows: (1) protrusion phase from first moment of tongue detection to the first volume change rate minimum; (2) retraction phase from the last volume change rate minimum to the last moment of tongue detection; (3) corrective submovement phase from protrusion phase offset to spout contact onset; (4) spout submovement phase from spout contact onset to retraction phase onset.

For kinematics variables, we calculated speed as the magnitude of the one-sample difference in the position vector; acceleration as the one-sample difference in speed; and pathlength by integrating the speed over the entire lick duration. The number of acceleration peaks was determined using MATLAB’s findpeaks function. The protrusion angle was defined as the angle between the facial midline and a vector pointing from a fiducial point on the jaw to the tongue tip (Fig. 1c). The facial midline was defined as the line that passes through the midpoint between the nostrils and the midpoint between the incisors. The fiducial lies on the midline and was calibrated for each individual mouse to be at approximately the same distance posterior to the mouth, aligned in the AP direction with the visible base of the jaw.

When examining the kinematics of any lick, we excluded trials in which the mouse contacted the spout twice or missed the spout on any

lick before the lick being analysed. To calculate the correlation between L2 contact location on the tongue and the protrusion angle change on the next lick, we first calculated the protrusion angle change (the difference in the protrusion angle from L2 to L3 for all trials; Extended Data Fig. 7a). We then correlated the L2 contact angle with the L2 to L3 protrusion angle change across all conditions (Extended Data Fig. 7c), as well as for each condition separately (Extended Data Fig. 7d–f).

Tongue contact location tracking. To create a 3D model of the spout, we first identified all of the discrete spout positions (for example, left, centre, right) used in a single behavioural session using example frames from videos of that session. We then used recorded command voltages sent to the servo motors to infer the 3D location of the spout tip in all other video frames from that session. Given the 3D spout location and the known size (0.072 inch outer diameter) and shape (cylinder) of the spout, we generated a full voxel representation of the spout for each frame.

For these analyses, we used spout contact sensor data to identify the set of video frames corresponding to the entire duration of the tongue–spout contact event on each lick. To identify which parts of the tongue surface contacted the spout, we first embedded the 3D representation of the spout in the same space as the 3D visual hull reconstruction of the tongue. We then performed an iterative search to identify which tongue voxels (each 60 μm³) were either overlapping with, or one voxel away from, spout voxels; these were defined as contact voxels. We then took the centroid of these contact voxels and defined this as the contact centroid. This was repeated for each timestep throughout the entire duration of tongue–spout contact for all licks that made contact with the spout. We next identified a similar facial landmark on the face of each mouse as a fiducial point.

To estimate the contact site on the tongue surface, we were mindful that the tongue is a highly deformable object without useful landmarks and, therefore, Euclidean positions on a fixed surface do not exist in the same way as for a finger or body, for example. Thus, we chose to quantify the contact site as a single variable, the contact angle. To obtain the contact angle for each lick, we calculated the angle between the tongue-tip vector (vector pointing from the fiducial to the tongue tip) and the contact centroid vector (vector pointing from the fiducial to contact centroid). We chose a polar coordinate system because it captures in a single angular measurement the variance in contact site in both mediolateral and anteroposterior axes that were elicited in our task. Note also that this method can estimate the contact site at every timestep during spout contact (that is, a contact trajectory); however, for analysis, we take the contact angle at the contact onset to reduce the trajectory to a single point. To assess head-centric tuning, we calculated head-centric contact angle as the angle between the contact centroid vector and the midline of the face (defined in the ‘Lingual kinematics analysis’ section above).

Analysis of optogenetic manipulations on lick kinematics. For bilateral and unilateral optogenetic manipulations, we analysed differences in L3 protrusion angle (Figs. 1f and 2d), and all other kinematic parameters (Extended Data Figs. 2e–j and 5a–f) between no-laser and laser conditions using a two-sided hierarchical bootstrap test. For unilateral optogenetic manipulations, we also calculated the angular correction magnitude (Fig. 2e) by taking the difference between the centre spout trial L3 protrusion angle and the contralateral or ipsilateral spout trial L3 protrusion angles for laser on and laser off trials. The difference between laser on and laser off trials was significant if the *P* value was less than 0.025 on either tail. Moreover, we compared the effect that inactivating each brain region (ALM, TJM1 or latSC) had on correction magnitude for ipsilateral or contralateral corrections separately using a two-sided hierarchical bootstrap test. We considered these as two sets of multiple comparisons, examining the *P* value against the Bonferroni-corrected *P* value ($P < 0.05/(3 \times 2) = 0.008$, three pairs of comparisons, tests on both tails).

For optogenetic stimulation experiments, we defined the protrusion angle for the first lick evoked by stimulation as the angle between the facial midline and a vector pointing from the fiducial point to the tongue tip at the moment of maximum tongue tip lateral displacement. We excluded data from sites that histology indicated may be outside the latSC or outside regions with viral expression (Extended Data Fig. 10a). We combined data with the same AP coordinates for each mouse. We then ran a correlation test between the AP coordinate of microstimulation sites and the median L1 protrusion angles for each animal, the results of which we report in Pearson's R^2 . We then examined whether the observed R^2 value was due to chance by performing a shuffle test, where the null distribution was created by shuffling condition (AP site) with L1 protrusion angle. These analyses were repeated for cue-only, stimulation-only and stimulation-with-cue experiments. To analyse L1 protrusion probability and latency across stimulation sites, we ran the Kruskal–Wallis test with Tukey's HSD post hoc test. We also analysed the differences between kinematic variables across cue-only, stimulation-only and stimulation-with-cue conditions using a two-sided hierarchical bootstrap test examining the P value against the Bonferroni-corrected P value ($P < 0.05/(3 \times 2) = 0.008$, three pairs of comparisons, tests on both tails). For analysis of the L1–L2 inter-lick interval, we included only trials in which L1 did not make spout contact and L2 was initiated during stimulation.

Electrophysiology analysis

Spike sorting and unit selection criteria. Extracellular voltage traces were first notch-filtered at 60 Hz. The data were then spike-sorted automatically with Kilosort2 (<https://github.com/MouseLand/Kilosort>)⁵³ and curated manually with Phy2 (<https://github.com/cortex-lab/phy>). Experimenters were blind to trial type during spike sorting. During manual curation, units containing low-amplitude spikes and/or non-physiological or inconsistent waveform shape were discarded and not included in further analyses. Neurons with fewer than ten trials in any of the conditions tested were excluded for all analyses performed below. Moreover, neurons that fired less than 0.1 Hz, either throughout the entire trial period or within a given time window defined in the sections below, were excluded from further analysis.

Rate histograms. The rate histograms for example neurons were computed by binning the spiking activity of each example neuron into 10 ms bins and aligning activity to the trial onset (Extended Data Fig. 3), L2 contact (Figs. 3a and Fig. 4c,d and Extended Data Figs. 6a and 8), L4 contact (Fig. 4c,d and Extended Data Fig. 8) or L4 protrusion onset (Extended Data Fig. 9a,e). For PCA of neural data, 5 ms bins were used to allow for a better estimate of divergence time and activity was aligned to L2 contact onset. Activity was smoothed by taking the moving average of the firing rate for each neuron in the preceding three time bins. To create rate heat maps across selectively modulated neurons, rate histograms for all selectively modulated neurons were computed as described above and data were aligned to L2 contact onset (Fig. 3b and Extended Data Fig. 6b). Selectivity for each neuron was determined as described below in the 'Single-unit significance testing' section. For each selectivity heat map, only neurons that were selectively modulated by a specific contact site (contralateral, centre and so on) were chosen for display. For all conditions within each selectivity heat map, neurons were sorted from top to bottom by the time of their peak mean firing rate within a 100 ms analysis window following L2 contact in the condition it was selective for. The firing rate of each neuron was min–max normalized in a window ± 300 ms around L2 contact. Note that, for some neurons, this means that the absolute peak firing rate for the neuron in the ± 300 ms window may have occurred outside of the selectivity analysis window. For photovalidation heat maps, rate histograms for each condition (laser on/off) were instead aligned to laser onset (Extended Data Fig. 3), min–max normalized and sorted in ascending order from top to bottom by the mean firing rate within the

laser on condition. Only neurons with a mean firing rate of >1 Hz within the analysis window on non-laser trials were included.

Single-unit significance testing. To determine whether the firing rate of a neuron was significantly modulated by the trial condition (left, centre, right) after L2 contact (Fig. 3a–c and Extended Data Fig. 6a,b), we calculated the firing rate in a 100 ms time window after L2 contact onset for each trial. We then performed a one-way analysis of variance (ANOVA) to test whether the firing rate of each neuron was modulated by condition. If a given neuron was significantly modulated by condition using ANOVA ($P < 0.05$), we then additionally performed pairwise post hoc tests (Tukey's HSD) to determine what condition pairs were significantly modulated with each other (left–right, left–centre, centre–right). A condition pair was significantly modulated if the P value was less than the Bonferroni-corrected P value ($P < 0.05/3$). A neuron was said to be selective for a given condition if the mean firing rate for a given condition was significantly greater than the mean firing rate in all other conditions. A neuron was said to be selective for two conditions if the mean firing rates for two conditions were significantly greater than the third, but those two conditions were not significantly different from one another.

To test whether the relative proportion of selective neurons differed by AP recording site in the latSC (Fig. 3c), we recorded the estimated AP/ML recording location within latSC during each recording session in a subset of our mice ($n = 4$ mice) using micromanipulator readings. Silicon probes were coated with either Dil or DiD on each session to verify the recording site. The specific dye used was alternated on each session. We then grouped neurons based on their recording location into five bins, spanning from -3.0 to $-3.8 (\pm 0.1)$ mm AP in the latSC, in 0.2 mm increments (for example, -3.0 mm AP includes sites spanning from -2.9 to -3.1 mm AP). To test whether the number of neurons selective for one particular condition was greater in proportion relative to other conditions, we performed a bootstrap test. We randomly sampled with replacement neurons from each recording site and assessed the proportion of selective neurons for each condition on each iteration for 100,000 iterations. The proportion of neurons selective for a particular condition (contralateral, for example) was said to be significantly greater than another condition (ipsilateral, for example) if the number of iterations where the proportion of neurons selective for the other condition (ipsilateral) was greater than the condition of interest (contralateral) was less than the Bonferroni-corrected P value ($P < 0.05/(2 \times 10) = 0.0025$).

To test whether a neuron was modulated during recentring trials on L4 (Extended Data Fig. 8b–f), we calculated the firing rate in a 100 ms time window after L4 contact onset for each trial. As recentring trials occurred only on left/right displacement trials, we performed two t -tests: one between the left and left recentring trials, and another between the right and right recentring trials. A neuron was modulated on L4 if either one of these tests had a P value of less than the Bonferroni-corrected P value ($P < 0.05/2$). To test whether a neuron was retuned from centre contacts on L2 to left or right contacts on L4, we included only neurons that were modulated by centre contacts on L2 ($n = 23$). To test whether a neuron was activated by both recentring trial types, we included only neurons that were L4 modulated ($n = 113$).

Contact location information of latSC neuronal activity. For these analyses (Fig. 3d), we excluded neurons with a mean firing rate of less than 3 Hz within the analysis window ($n = 422$ out of 553 neurons passed this criteria). To determine the amount of contact location information (in bits per spike) present in individual latSC cells, we repurposed analyses previously used to analyse spatial information in hippocampal place cells⁵⁴. In brief, contact location information was obtained from the following equation, where N is the total number of contact angle bins, p_i is the probability of occupancy, λ_i is the firing rate in the i th contact angle bin, and λ is the mean firing rate of the neuron:

Article

$$CI = \sum_{i=1}^N p_i \frac{\lambda_i}{\lambda} \log_2 \frac{\lambda_i}{\lambda}$$

To test whether a neuron was significant for contact location information, we performed a shuffle test. For each neuron, we randomly permuted contact angle relative to their respective binned firing rates 1,000 times and examined whether the observed contact location information value was outside of the 95th percentile of the shuffled distribution.

Correlating latSC neural activity with contact angle. We included only neurons with significant L2 selectivity for L2-only correlation analyses (Fig. 3a,e and Extended Data Fig. 6a), and only neurons with significant L2 and L4 selectivity for recentring analyses (Fig. 4e and Extended Data Fig. 8c). We also excluded neurons with a mean firing rate of less than 3 Hz in the analysis window for L2 correlation analyses ($n = 422$ out of 553 neurons passed this criteria). For neurons that passed this criteria, L2 (or L4) contact angles were binned by 3° (contact bins) and the mean firing rate after L2 contact in each contact bin was calculated. We required at least three trials in each bin for that bin to be included in the analysis. A correlation was considered to be significant if the actual R^2 is greater than the 95th percentile of R^2 values obtained by permuting the firing rate with respect to contact angle over 1,000 iterations. We calculated head-centric contact angles as the angle between the contact vector and the facial midline (which passes through the fiducial), both in the bottom view.

PCA of latSC population activity. To obtain an estimate of when neural activity on left and right trials diverged from centre trials (Fig. 3f), we first used PCA to reduce the dimensionality of our data as previously described^{8,55}. Data were aligned to L2 contact onset, and peri-stimulus time histograms were generated in 5 ms bins to create a matrix of (neurons \times time bins \times conditions). We then ran PCA on these data and projected the condition-averaged (left, centre and right) responses onto the first 19 dimensions of this space, which together explained $>90\%$ of the neural variance in our dataset. The neural distance was calculated as the Euclidean distance between the left and centre or right and centre trajectories in the first 19 dimensions. We plotted the trajectories from each condition in the first three dimensions of this space (Fig. 3f (left)), in addition to the median times of behavioural variables, such as the time of L2 contact, on these trajectories.

To obtain the time of divergence between trajectories, as well as an estimate of the variability of these distances, we performed a hierarchical bootstrap. For each condition (left, centre and right), we first resampled with replacement neurons, and then resampled with replacement trials for each condition. We then computed peri-stimulus time histograms with this resampled dataset, projected the data onto the top 12 principal components and again calculated the Euclidean distance between the left and centre and right and centre trajectories. This procedure was repeated 1,000 times to yield the bootstrapped estimate of the s.d. of the distance between these trajectories. The time of divergence between neural trajectories was then defined as the median time that the neural distance exceeded 2 s.d. above the mean baseline activity (-300 to 0 ms before L2 contact onset) across both left/centre and right/centre bootstraps.

Contact response latencies of single latSC neurons. For determining the L2 response latencies of latSC neurons (Fig. 3g), we restricted our analyses to only neurons with significant L2 selectivity. For each neuron, we aligned neural activity to L2 contact onset in 1 ms bins and performed Wilcoxon rank-sum tests on the number of spikes in 5 ms windows across: (1) left versus right; (2) left versus centre; and (3) centre versus right conditions, similar to previous analyses used for estimating neuronal response latencies to distorted auditory feedback in singing birds⁵⁶. Windows were shifted in 3 ms increments from 0 – 250 ms

relative to L2 contact onset. The response latency was defined as the first bin where at least three consecutive bins had a Bonferroni-adjusted $P < 0.0055 = (0.05/(3 \times 3))$, 3 conditions, 3 bins.

To examine the response latency of latSC neurons (Extended Data Fig. 8h) depending on coordinate frame (tongue centric and so on), we first determined the coordinate frame, or lack thereof, of each latSC neuron by correlating neural activity after L4 contact with the contact location in either a tongue- or head-centred reference frame, as described in the ‘Correlating latSC neural activity with contact angle’ section. For these analyses, we included only neurons recorded during recentring sessions and with significant L2 and L4 selectivity. We then calculated the median response latency across all neurons of a given reference frame and performed a hierarchical bootstrap over 1,000 iterations for significance testing and to get an estimate of the IQR. Response latencies in a head-centric reference frame were considered to be significantly longer than latencies in another reference frame if the P value was lower than the Bonferroni-adjusted P value of <0.016 ($0.05/3$).

Lick cycle cross-correlation analysis. To determine whether the activity of a neuron was correlated with lick cycle (Extended Data Fig. 9a–c), we analysed the time window from 50 ms before L4 protrusion onset to 300 ms after L4 protrusion onset in non-recentring trials only. We chose L4 for this analysis because the spiking of latSC neurons before L4 was often dominated by L2 contact and L3 re-aiming responses, and we chose non-recentring trials to ensure recentring contacts would not similarly dominate L4 responses. We calculated the average firing rate and tongue volume across trials with a 10 ms bin size for the left, centre and right trials separately. Only bins with at least 10 trials were included in this analysis. Neurons with a firing rate lower than 5 Hz during the analysis window were excluded. Cross-correlation was then performed between the mean-subtracted firing rate of a neuron and tongue volume with normalization. The lag was determined as when the maximum cross-correlation coefficient was obtained within a ± 100 ms lag window (Extended Data Fig. 9d). For each trial type, a neuron was considered significantly correlated with the lick cycle if the first percentile of the bootstrapped maximum cross-correlation coefficient values was greater than the median shuffled maximum cross-correlation coefficient values obtained by randomizing spike time within each trial. Both the bootstrap and randomization were performed over 1,000 iterations.

Encoding model analysis. We used Poisson GLMs to determine whether the activity of single latSC neurons encoded tongue position information before L4 contact (Extended Data Fig. 9f–i). Note that we are using GLMs as an analysis method to examine coding of tongue position in the latSC, not as a model of the latSC per se. Inspired by previous work^{57,58}, we sought to make predictions of latSC neuronal activity on single licks, rather than across an arbitrary time window before L4 contact. We summed the number of spikes on each trial from 50 ms before L4 protrusion onset until L4 contact onset and computed two families of features for each protrusion: tongue tip position at L4 protrusion offset ($x/y/z$ components) and previous (L3) spout contact location ($x/y/z$ components). Although we were most interested in testing whether tongue position was encoded in pre-contact L4 latSC neuronal activity, given the close temporal proximity (-120 ms) between past (L3) contact and L4 re-aiming, any relationship we might observe between L4 tongue position and latSC neuronal activity could be confounded by past L3 contact location. We included both variables to examine whether L4 tongue position was better encoded than past L3 contact location in latSC pre-contact L4 activity. We also included two other predictors: protrusion duration before L4 contact and an estimate of firing rate drift over the session. Protrusion duration before L4 contact was included, as any difference in duration between trial types could give rise to spurious correlations with tip position. We estimated drift

by dividing the trials over a session into five equally sized chunks and computing the mean firing rate in each chunk. We took the log of both predictors to account for the exponential nonlinearity. For these analyses, only neurons with a firing rate greater than 5 Hz during the analysis window were included ($n = 320$ out of 553 neurons).

We fitted GLMs with the ‘fitglm’ function in MATLAB, using an exponential link function. We used fivefold cross-validation to assess the goodness-of-fit of our models. Goodness-of-fit was assessed using McFadden’s pseudo- R^2 , which was calculated on held-out test data on each fold of cross-validation and averaged across all folds. Note that pseudo- R^2 values of 0.2–0.4 represent excellent fits.

We included in our analyses a null model that consisted only of protrusion duration before L4 contact and firing rate drift as predictors. To test for significance between the full and null model, we first calculate the likelihood ratio test statistic in the observed data. We then calculated this same statistic on 1,000 instances of shuffled data, where the rows of the design matrix were permuted relative to spiking activity. A neuron was included in the further analysis if the probability of the shuffled likelihood ratio being greater than the actual likelihood ratio was less than a P value of 0.05. To test for significance of each variable, we repeated the above analysis, except between the log-likelihood of the full model and each partial model. A neuron was considered to be significant for a predictor if the probability of the shuffled likelihood ratio being greater than the actual likelihood ratio was less than the Bonferroni-corrected P value ($P < 0.05/6$).

The relative contribution of each predictor for each neuron was calculated as previously described^{57,58} from the following equation, where $R_{p,i}^2$ is the variance explained by the partial model excluding the i th predictor and R_f^2 is the variance explained by the full model:

$$RC = \left(1 - \frac{R_{p,i}^2}{R_f^2}\right) / \sum_{j=1}^5 \left(1 - \frac{R_{p,j}^2}{R_f^2}\right)$$

Relative contributions were averaged across all neurons to create Extended Data Fig. 9h.

Statistics

We performed t -tests, correlation, linear regression, Kruskal–Wallis, likelihood ratio and ANOVA tests using built-in functions of MATLAB. Shuffle tests were used for behaviour and photomanipulation analyses. We performed hierarchical bootstrapping where required by resampling mice with replacement, then resampling trials with replacement within each condition. The parameter (such as mean, median) or statistic of interest was then calculated on each round of bootstrapping. We performed shuffle tests by randomly permuting data from one of two variables while keeping the other fixed, and calculating the test statistic (such as correlation coefficient) on each iteration to create a null distribution.

Reporting summary

Further information on research design is available in the Nature Portfolio Reporting Summary linked to this article.

Data availability

Source data have been deposited at an Open-Science Framework (OSF) repository (<https://doi.org/10.17605/OSF.IO/FY7J5>). Source data are provided with this paper.

Code availability

Custom MATLAB and Python code used for analysis is available at GitHub (<https://github.com/GoldbergLab/Ito-Gao-et-al-2024>).

51. Osborne, J. E. & Dudman, J. T. RIVETS: a mechanical system for in vivo and in vitro electrophysiology and imaging. *PLoS ONE* **9**, e89007 (2014).
52. Hayar, A., Bryant, J. L., Boughter, J. D. & Heck, D. H. A low-cost solution to measure mouse licking in an electrophysiological setup with a standard analog-to-digital converter. *J. Neurosci. Methods* **153**, 203–207 (2006).
53. Pachitariu, M., Sridhar, S., Pennington, J. & Stringer, C. Spike sorting with Kilosort4. *Nat. Methods* **21**, 914–921 (2024).
54. Skaggs, W., McNaughton, B. & Gothard, K. An information-theoretic approach to deciphering the hippocampal code. In *Advances in Neural Information Processing Systems* 5 (eds Hanson, S., Cowan, J. & Giles, C.) 1030–1038 (NIPS, 1992).
55. Ames, K. C., Ryu, S. I. & Shenoy, K. V. Simultaneous motor preparation and execution in a last-moment reach correction task. *Nat. Commun.* **10**, 2718 (2019).
56. Chen, R. et al. Songbird ventral pallidum sends diverse performance error signals to dopaminergic midbrain. *Neuron* **103**, 266–276 (2019).
57. Engelhard, B. et al. Specialized coding of sensory, motor and cognitive variables in VTA dopamine neurons. *Nature* **570**, 509–513 (2019).
58. Rodgers, C. C. et al. Sensorimotor strategies and neuronal representations for shape discrimination. *Neuron* **109**, 2308–2325 (2021).

Acknowledgements We thank C. Rodgers for advice on GLMs; M. Warden for use of the Zeiss LSM 710 confocal microscope; T. Bollu, J. Fatcho, A. Pruszynski, M. Sheehan, M. Warden and the members of the J.H.G. laboratory for discussions; and T. Bollu, A. Fernandez-Ruiz, J. Fatcho, G. Maimon, A. Oliva, M. Sedigh-Sarvestani and M. Zipple for comments on the manuscript. This work was supported by the NIH Director’s New Innovator Award (1DP2HD087952-01), an NIH NINDS R01 (1R01NS138093-01) and Jean Sheng and the Sheng Family Foundation. B.S.I. was supported by an NSF Graduate Research Fellowship.

Author contributions B.S.I., Y.G. and J.H.G. designed the experiments. B.S.I. and Y.G. trained all of the animals, conducted all experiments and analysed all data. B.S.I. and B.K. developed the contact location tracking algorithms. B.S.I., B.K. and Y.G. built the hardware and software necessary for data acquisition. B.S.I. and J.H.G. wrote the manuscript.

Competing interests The authors declare no competing interests.

Additional information

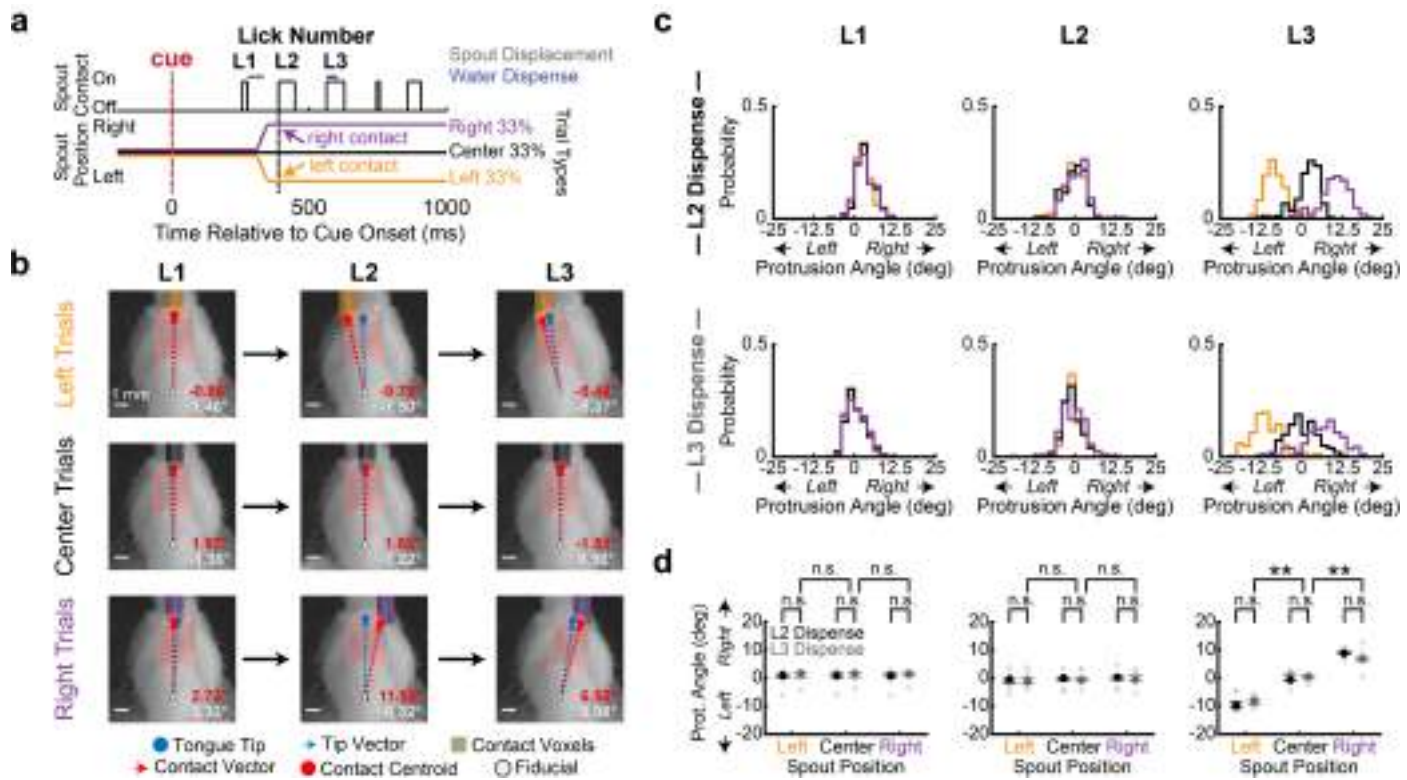
Supplementary information The online version contains supplementary material available at <https://doi.org/10.1038/s41586-024-08339-3>.

Correspondence and requests for materials should be addressed to Brendan S. Ito or Jesse H. Goldberg.

Peer review information *Nature* thanks Scott Pluta and the other, anonymous, reviewer(s) for their contribution to the peer review of this work. Peer reviewer reports are available.

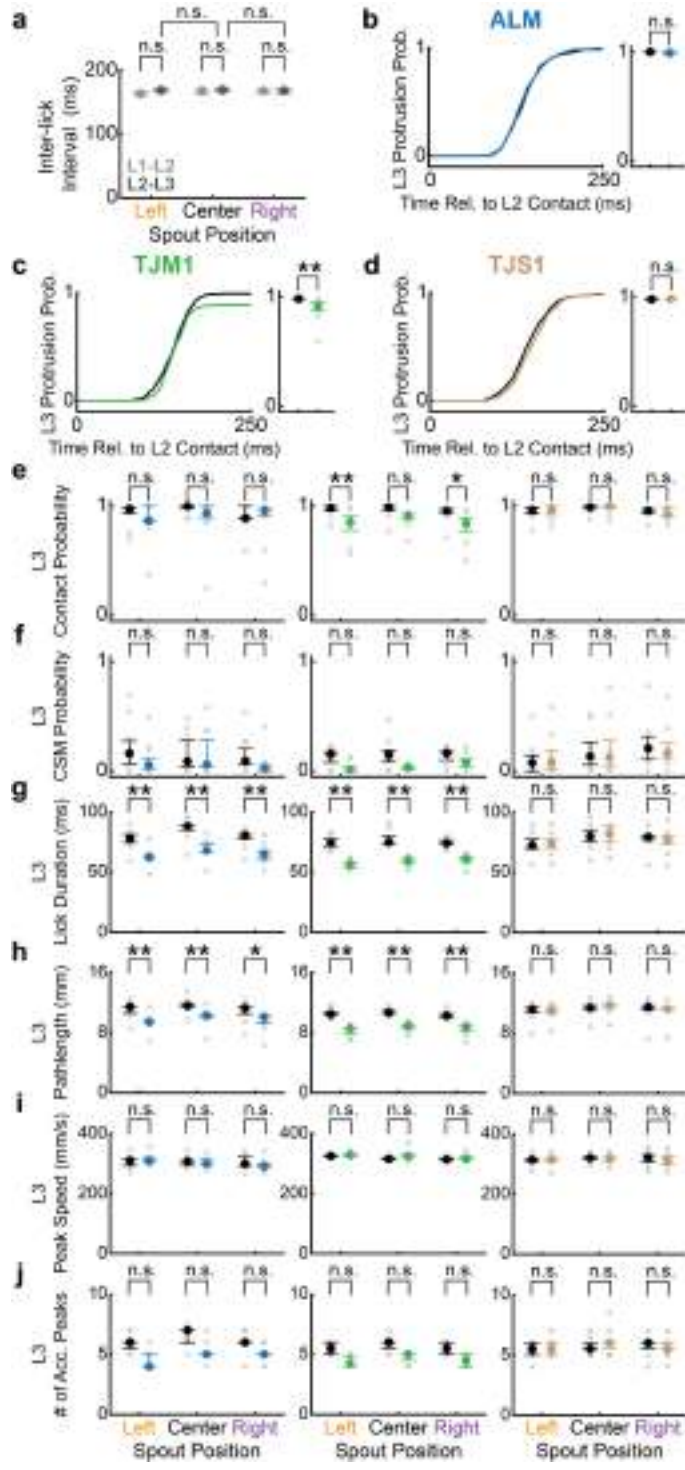
Reprints and permissions information is available at <http://www.nature.com/reprints>.

Article

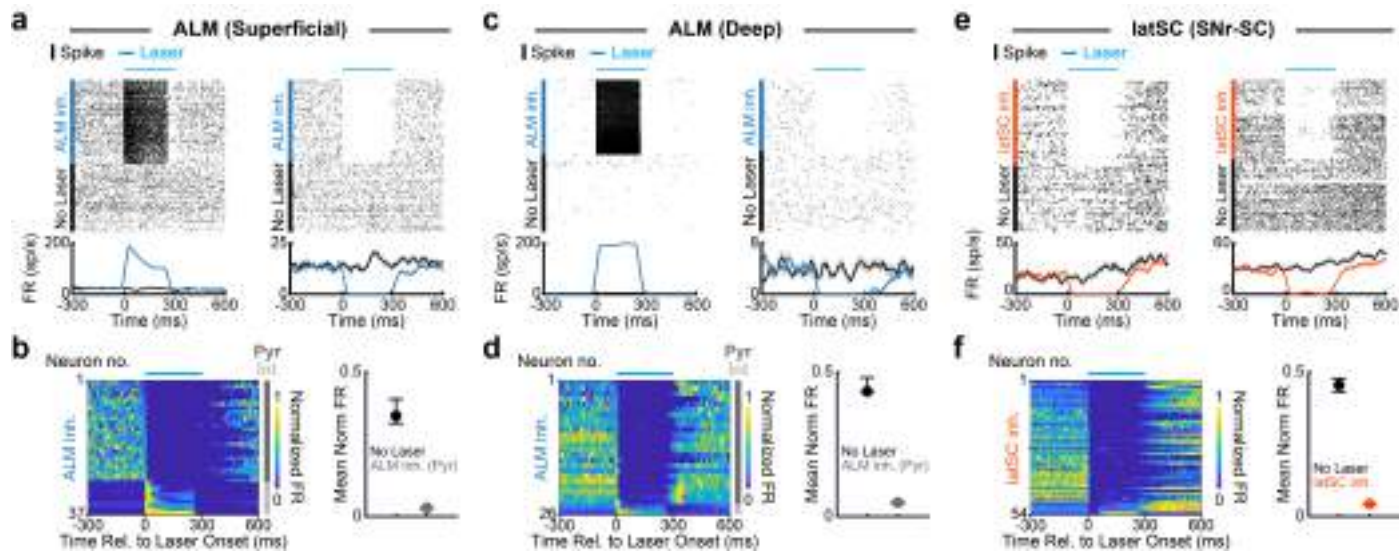


Extended Data Fig. 1 | Touch-guided re-aiming does not depend on water dispensation. **a**, Trial structure was the same as in Fig. 1a, except water was dispensed at L3 contact instead of L2 contact. **b**, Bottom view still frames at L1-L3 contact onset across trial types for dispense on L3 trials. Tip site and vector, blue dot and dashed line. Contact site and vector, red dot and dashed line. Contact angle and protrusion angle, red and white values. **c**, L1-L3 protrusion

angle distributions during left (gold), centre (black) and right (purple) trials from a session where water was dispensed on L2 (top) or L3 (bottom). **d**, L3 protrusion angles for dispense on L2 (black, $n=7$ mice) and dispense on L3 trials (dark grey, $n=7$ mice). Grey dots are medians of individual mice. Data in **d** are median \pm IQR. **corrected $p < 0.01$, two-sided hierarchical bootstrap test; n.s., not significant. Exact statistics are in Supplementary Table 2.

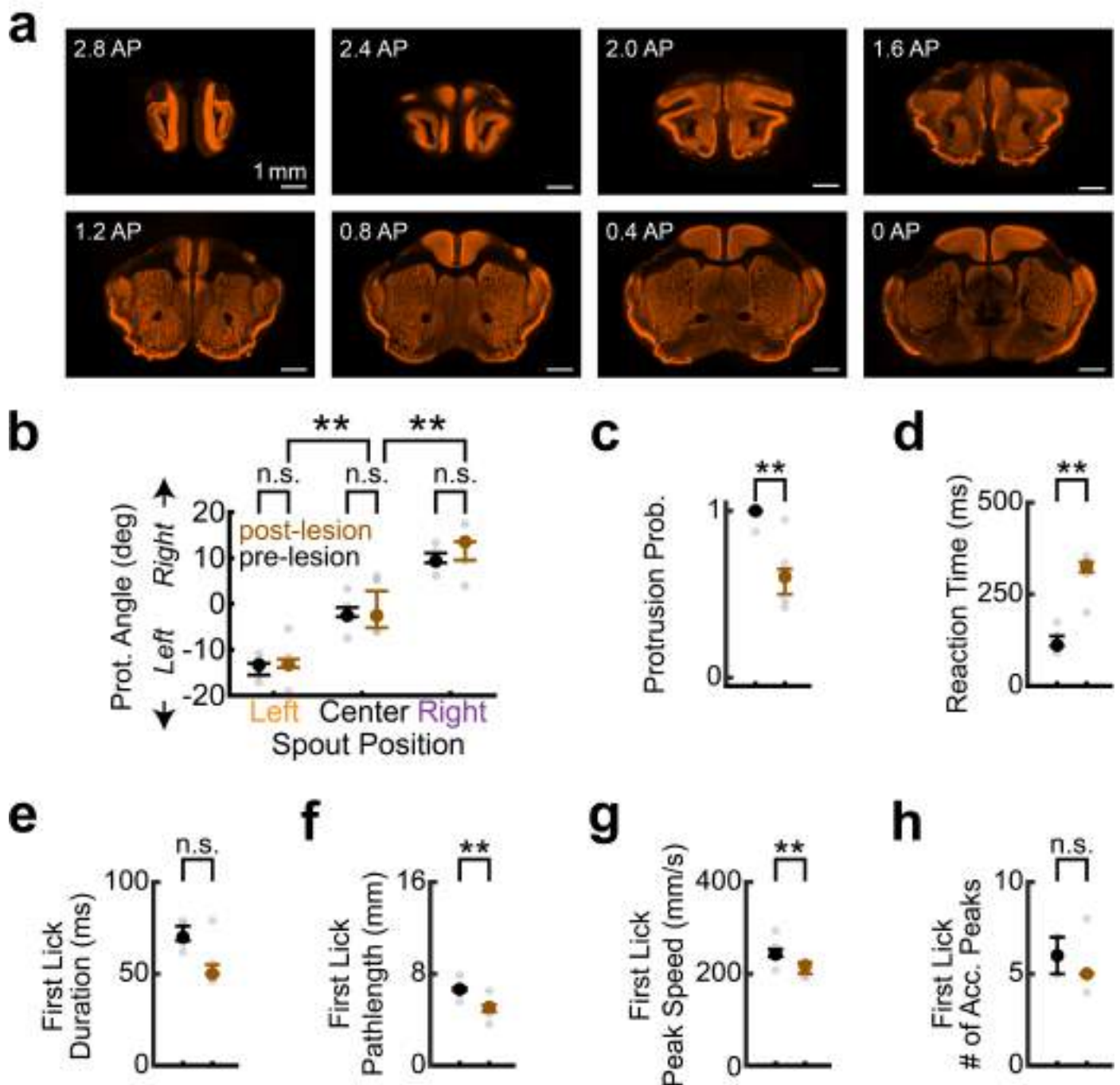


Extended Data Fig. 2 | Bilateral photoactivation of ALM and TJM1, but not TJS1, reduces lick pathlength and duration. **a**, Rhythm of lick bouts are unaffected by spout displacement on L2. Inter-lick intervals (ILI) for L2 to L3 (dark grey) do not significantly differ by condition. ILI for L1 to L2 (light grey), where no spout displacements occurred, provided for comparison. **b-d**, Left, Cumulative probability of L3 protrusion relative to L2 contact onset for ALM (blue, **b**), TJM1 (green, **c**) and TJS1 (brown, **d**) inactivated trials, relative to no laser trials for the same mice (black). Right, L3 protrusion probability for inactivation and no laser trials. **e-j**, Effect of bilateral ALM, TJM1 or TJS1 inactivation on L3 lick kinematics. L3 contact probability (**e**), corrective submovement (CSM) probability (**f**), lick duration (**g**), lick pathlength (**h**), lick peak speed (**i**) and number of acceleration peaks (**j**) for left, centre and right trials. Colours for each panel are the same as in **b-d**. Note that ALM and TJM1, but not TJS1, inactivation impair lick duration and pathlength. Data in **e-j** are median \pm IQR. *corrected $p < 0.05$, **corrected $p < 0.01$, two-sided hierarchical bootstrap test; n.s., not significant. Exact statistics are in Supplementary Tables 1, 3 and 4.



Extended Data Fig. 3 | Electrophysiological validation of photoinhibition of the cortex and latSC. **a**, Spike rasters (top row) and rate histograms (bottom row) for an example putative interneuron (left) and pyramidal neuron (right) recorded in the superficial layers of ALM during photovalidation experiments in VGAT-CHR2-EYFP mice. Data are aligned to trial onset and sorted by laser on (dark blue) or off (black) trials. Cyan bar above the raster indicates when the laser was on. Laser power, waveform and duration were the same as in behavioural experiments. **b**, Left, Normalized mean \pm IQR firing rates of superficial layer ALM neurons (300–800 μ m below dura surface, Methods) recorded during

photoinactivation. Dark grey and light grey indicate putative pyramidal and interneurons, respectively. Right, Mean \pm IQR normalized firing rate of putative ALM pyramidal neurons during no laser (black) and laser on (dark grey) trials. **c-d**, Same as **a-b**, but for an example putative interneuron (left) and pyramidal neuron (right) recorded in the deep layers of ALM (800–1200 μ m below dura surface, Methods). **e-f**, Same as **a-b**, but for two example neurons recorded in latSC during axonal stimulation of the SNr-SC pathway in Vgat-cre mice (orange). For all rate histograms, shading represents the bootstrapped s.e.m. across trials.

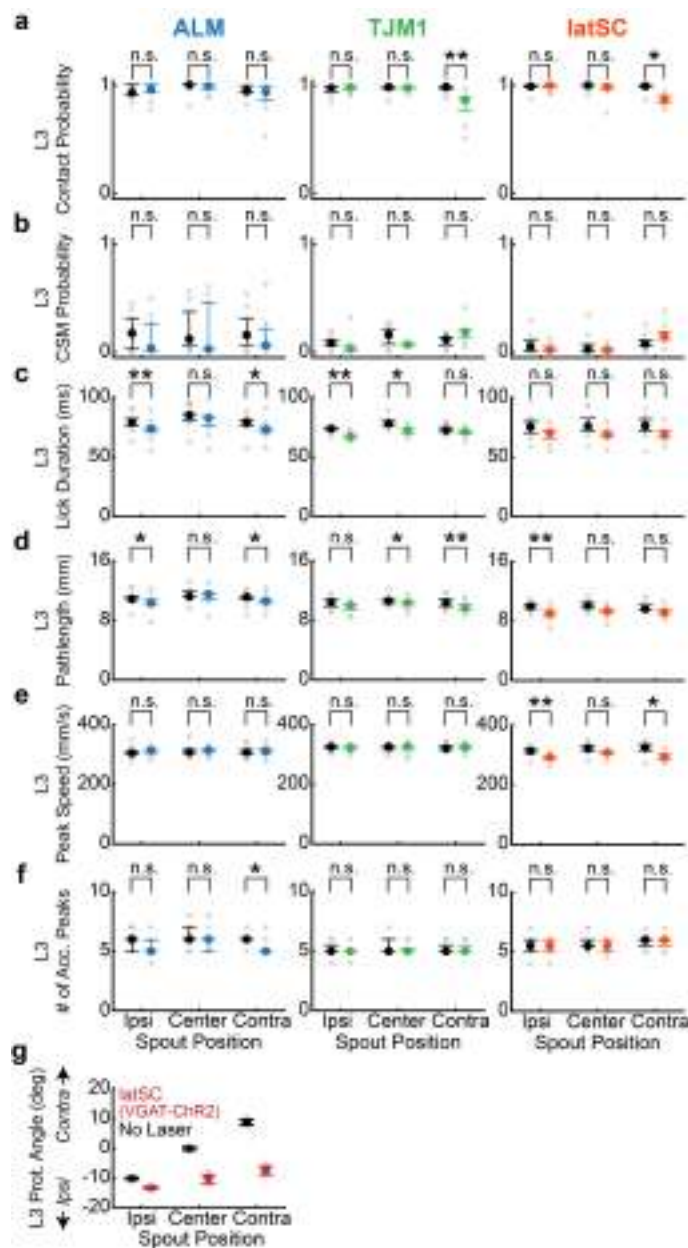


Extended Data Fig. 4 | Lesions of all three lingual cortical areas at once impair lick kinematics while preserving touch-guided re-aiming.

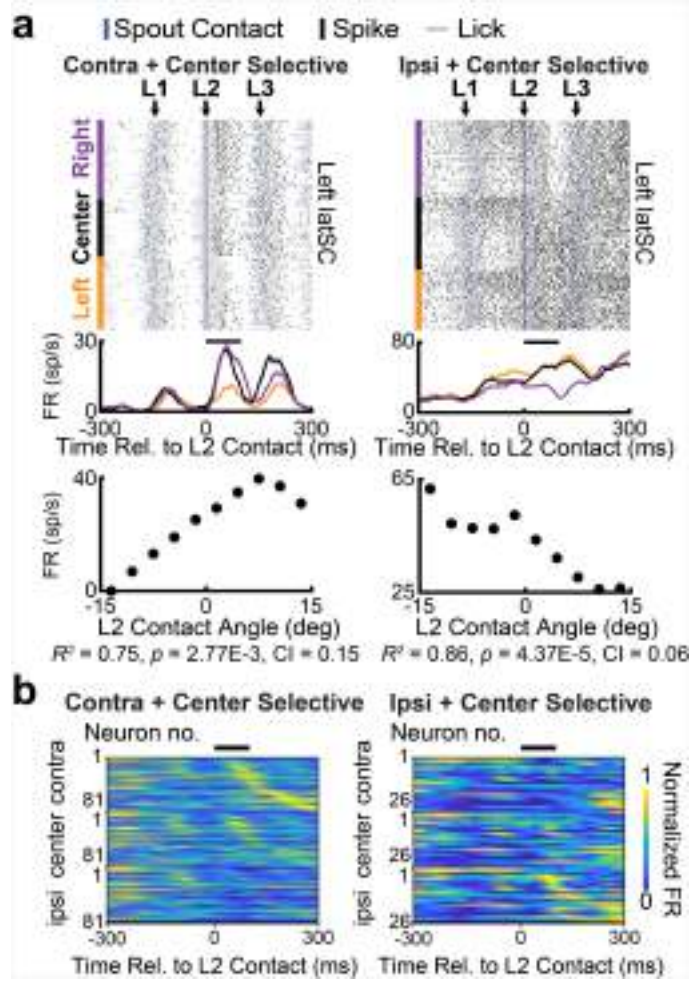
a, Example histological images from a mouse with ALM, TJM1 and TJS1 lesioned. Slices were stained with anti-NeuN (gold). Scale bar, 1 mm. b-h, L3 protraction angles (b), protrusion probability (c), reaction time (d), first lick duration (e),

first lick pathlength (f), first lick peak speed (g), and first lick number of acceleration peaks (h) across mice prior to lesion (black) and post-lesion (brown). Data in b-h are median \pm IQR, $n = 5$ mice. *corrected $p < 0.05$, **corrected $p < 0.01$, two-sided hierarchical bootstrap test; n.s., not significant. Exact statistics are in Supplementary Tables 5 and 6.

Article

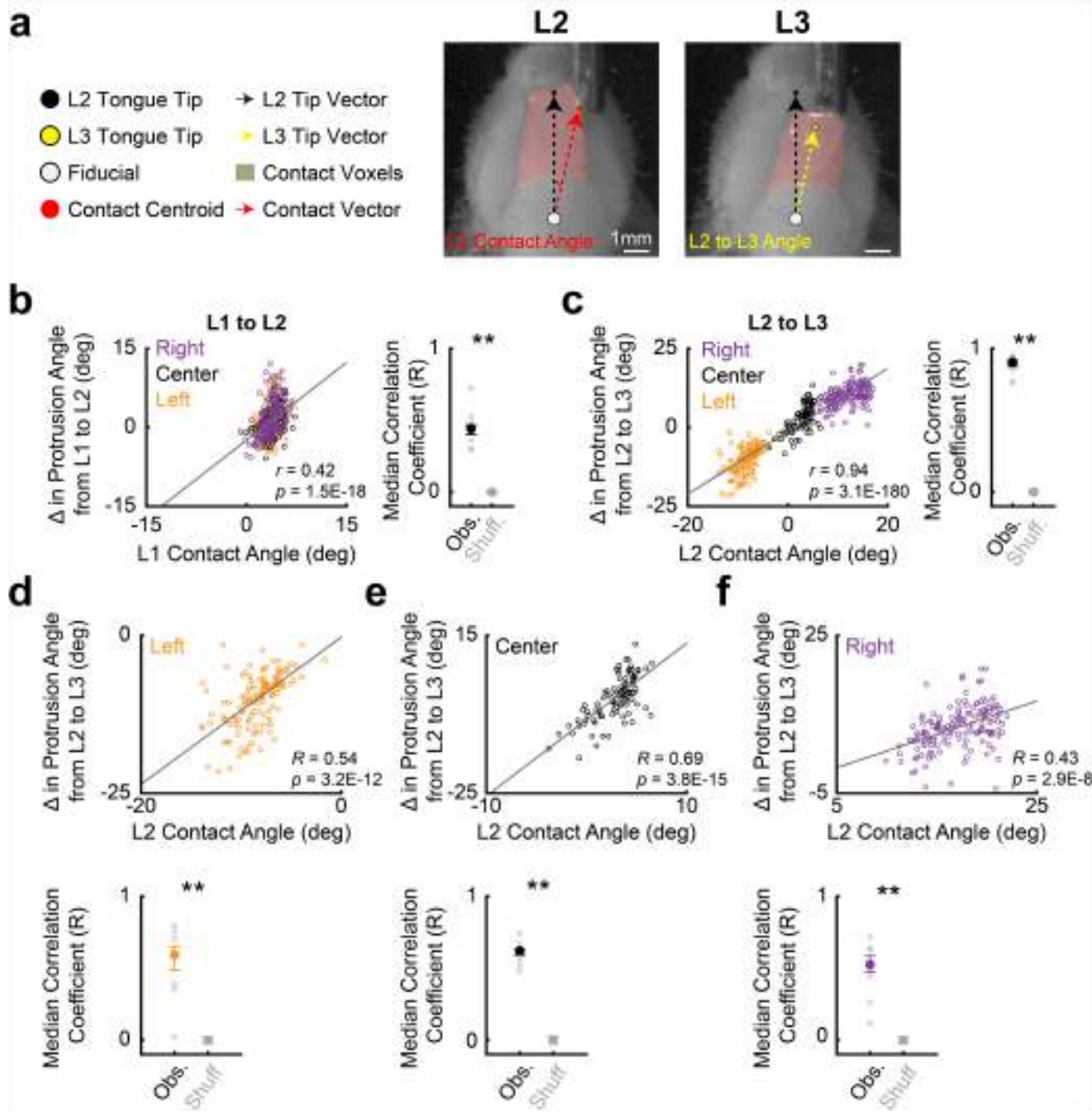


Extended Data Fig. 5 | Unilateral photoactivation of ALM, TJM1 and latSC minimally impairs L3 kinematics. **a-f.** Effect of unilateral ALM, TJM1 or latSC inactivation on L3 lick kinematics for left, centre and right trials. **a.** L3 contact probability. **b.** Corrective submovement (CSM) probability. **c.** Lick duration. **d.** Lick pathlength. **e.** Lick peak speed. **f.** Number of acceleration peaks. Data in **a-f** are median \pm IQR. Colours in **a-f** correspond to the photoactivated brain region. **g.** Effect of unilateral inactivation of latSC on L3 protrusion angles in VGAT-ChR2-eYFP mice ($n = 2$). Note that, like unilateral latSC photoactivation in Vgat-cre mice targeting the SNr-SC pathway, unilateral latSC inactivation in VGAT-ChR2-eYFP mice impaired contralateral re-aiming. Black dots are no laser trials from the same session. Grey dots are medians of individual mice. * $p < 0.05$, ** $p < 0.01$, two-sided hierarchical bootstrap test; n.s., not significant. Exact statistics are in Supplementary Table 7.



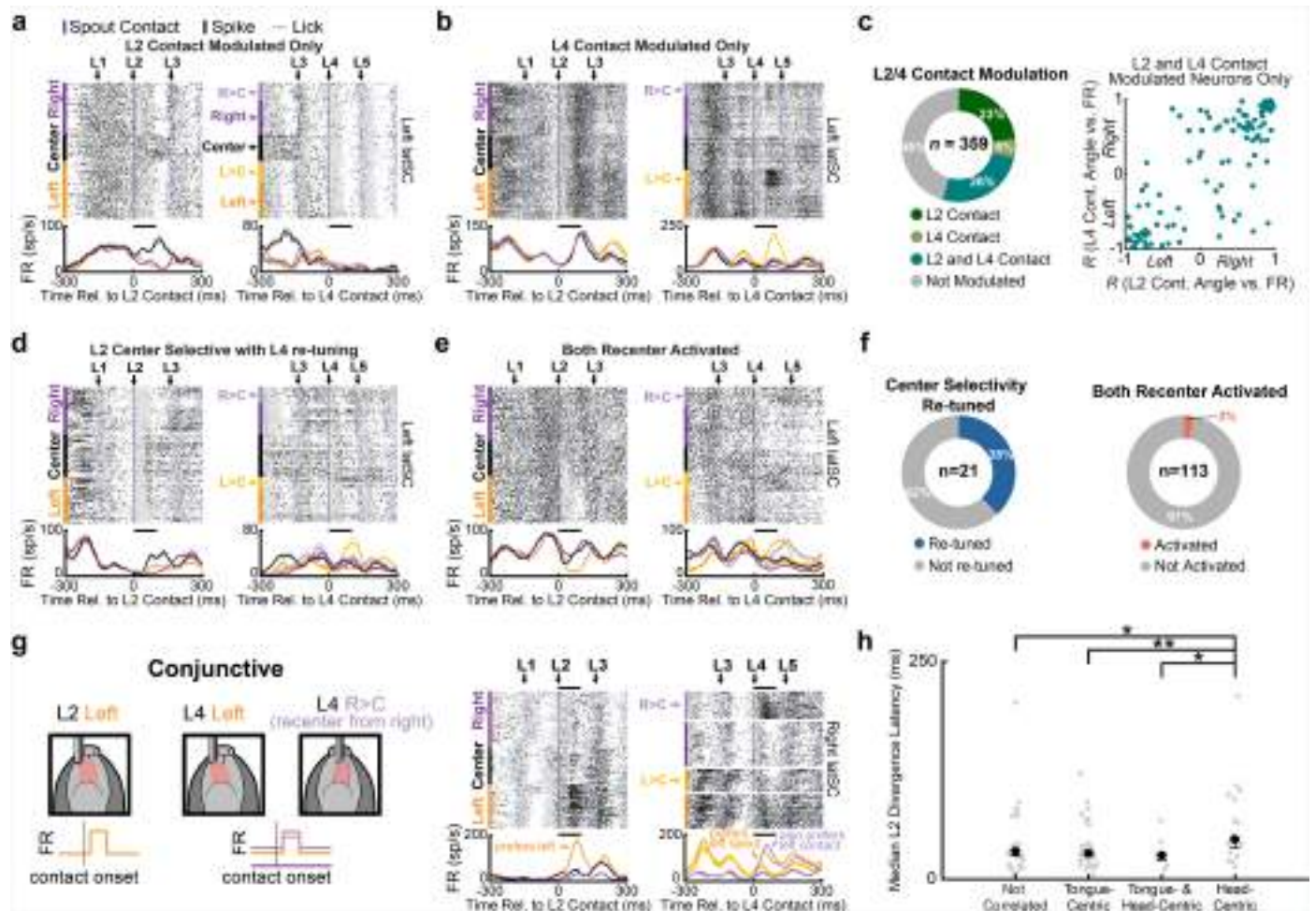
Extended Data Fig. 6 | latSC neurons exhibit diverse tuning in response to contact events. **a**, Spike rasters (top row), rate histograms (middle row) and relationship between mean firing rate and L2 contact angle (bottom row) for contralateral + centre (left), ipsilateral + centre (middle). Data are sorted by condition, then by L2 contact angle within each condition. Shading represents the bootstrapped s.e.m. across trials. **b**, Normalized mean firing rates of L2-contact modulated neurons with significant selectivity for contralateral + centre (left, $n = 81/279$) and ipsilateral + centre (right, $n = 23/279$) contacts on L2.

Article



Extended Data Fig. 7 | Location of contact events on the tongue predicts next lick re-aiming. **a**, Example still frames of L2 and L3. Contact angle for each lick was defined as the angle between the tip vector (pointing from fiducial to tongue tip) and the contact vector (pointing from fiducial to contact centroid). Protrusion angle change was defined as the angle between the tip vectors at time of spout contact for one lick and the next. **b**, Example data from a single session showing that L1 contact angle (which varied slightly even though the spout was always centred) was significantly correlated with the change in protrusion angle from L1 to L2 across trial types (left). Pearson's R and p -value for example data shown in inset. **c**, Same as **b**, but for correlation between L2 contact angle and the change in protrusion angle from L2 to L3 across trial types. Colours as in **b**. **d-f**, Same data as **c** but analysed separately for each condition: left (**d**), centre (**e**), and right (**f**). Top, example data. Bottom, median correlation coefficient compared to shuffled data. ** $p < 0.01$, two-sided shuffle test. Exact statistics are in Supplementary Table 11.

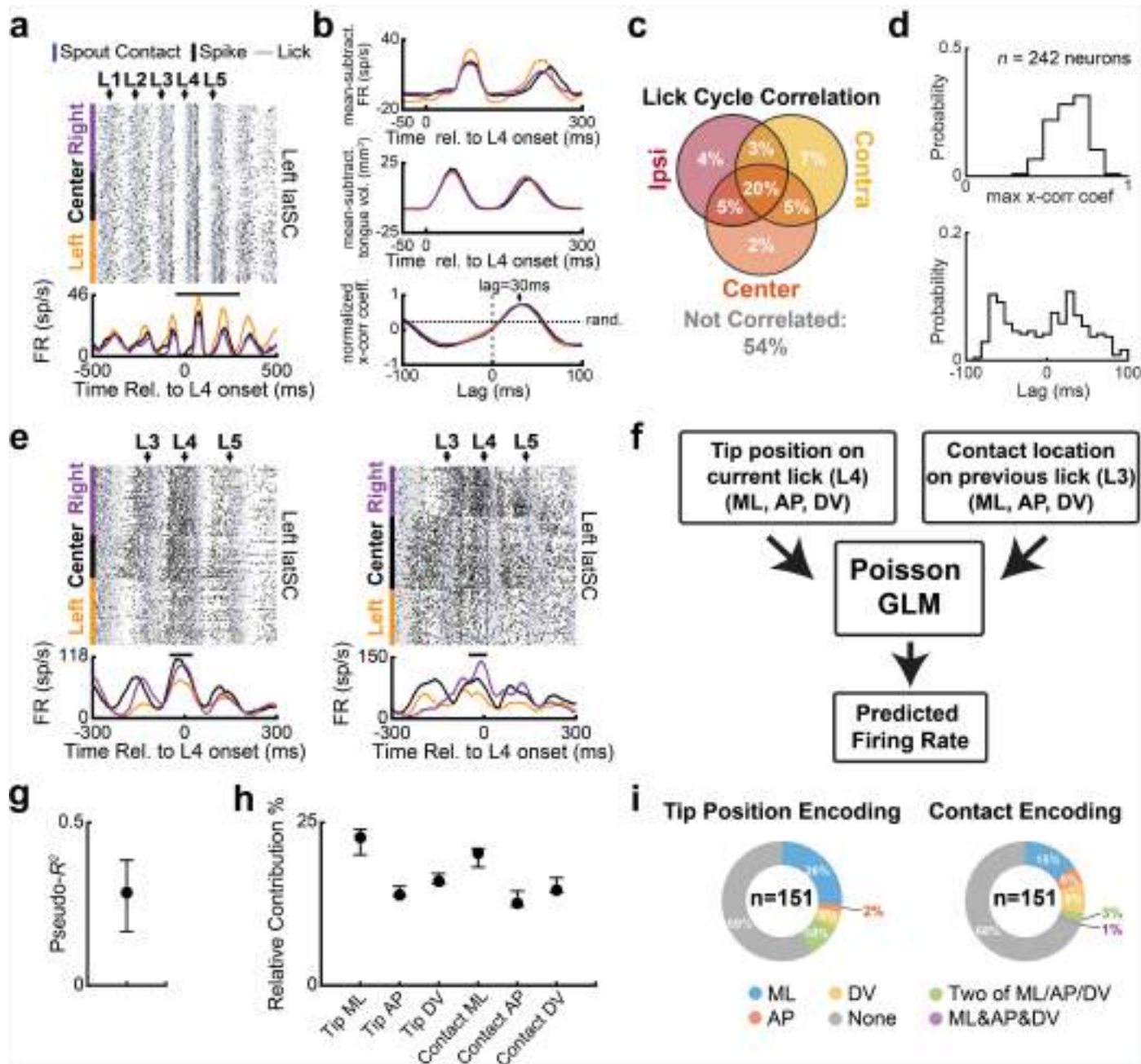
linear regression. Right, median correlation coefficient (Pearson's R , black) compared to shuffled data (grey, $n = 6$ mice). Left, centre and right displacement trials are yellow, black and purple, respectively. Pearson's R and p -value for example data shown in inset. **c**, Same as **b**, but for correlation between L2 contact angle and the change in protrusion angle from L2 to L3 across trial types. Colours as in **b**. **d-f**, Same data as **c** but analysed separately for each condition: left (**d**), centre (**e**), and right (**f**). Top, example data. Bottom, median correlation coefficient compared to shuffled data. ** $p < 0.01$, two-sided shuffle test. Exact statistics are in Supplementary Table 11.



Extended Data Fig. 8 | latSC neuronal activity can be selectively tuned to contact events on some licks, but not others. a–b. Example latSC neurons tuned to contacts on specific licks. **a.**, A neuron tuned to certain contact locations during L2, but not L4. **b.**, A neuron tuned to certain contact locations during L4, but not L2. **c.**, Left, Percentage of L2- and L4-modulated neurons tuned to contacts on L2 only (dark green), L4 only (light green), both L2 and L4 (green), or neither L2 or L4 (grey). Right, Pearson's R between L2 contact angle and mean firing rate following L2 contact plotted against Pearson's R for L4 contact angle and mean firing rates following L4 contact. Positive and negative correlation coefficients indicate right or left preference, respectively. Note that the activity of many latSC neurons exhibited similar correlations between firing rate and contact location on L2 and L4. **d.**, Example latSC neuron selective for L2 centre contacts that was re-tuned to non-centre responses on L4 during recentering trials. **e.**, Example L4 modulated neuron that was activated by both left and right recentering trials. **f.**, Left, Percentage of neurons selective for L2 centre contacts that were re-tuned to a non-centre contact on L4 (blue). Blue

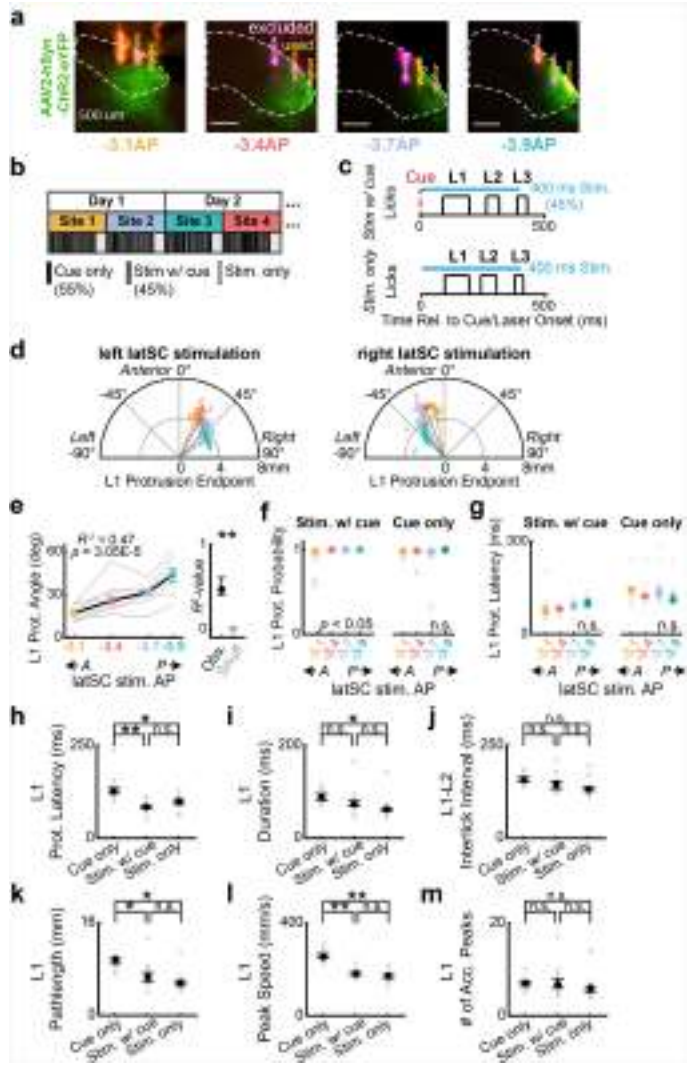
and grey, re-tuned and not re-tuned, respectively. Right, Percentage of L4 modulated neurons that were activated by both left and right recentering trials (orange). **g.**, Left, Illustration of a hypothetical conjunctively-tuned neuron. Right, Spike rasters and rate histograms for an example conjunctively-tuned latSC neuron aligned to L2 (left) and L4 contact (right). Colours as in Fig. 1a. **h.**, Median \pm IQR of single neuron divergence latencies between left, centre and right conditions for tongue-, head-, and conjunctively-tuned neurons, as well as neurons that were not correlated with any reference frame. Note that tactile responses in neurons with a head-centric reference frame diverged significantly later than those with tongue-centric ($p = 0.003$) or conjunctive ($p = 0.007$) reference frames, as well as neurons that were modulated, but not correlated ($p = 0.006$), with contact site. Grey dots are individual neuron divergence latencies. *corrected $p < 0.05$, **corrected $p < 0.01$, one-sided hierarchical bootstrap test. For all rate histograms, shading represents the bootstrapped s.e.m. across trials. **g** was adapted from ref. 8 (Springer Nature Limited).

Article



Extended Data Fig. 9 | latSC neuronal activity prior to spout contact encodes tongue position. **a**, Example lick cycle correlated latSC neuron. Black bar indicates window used for cross-correlation analysis. **b**, Top, Mean-subtracted firing rate of the neuron in **a**. Middle, Mean-subtracted tongue volume. Data in **a** and **b** are aligned to L4 protrusion onset. Bottom, Normalized cross-correlation coefficient histogram. Black horizontal line, correlation coefficient from shuffled data. **c**, Percentage of neurons correlated with lick cycle across all combinations of trial types. Note that the circles are not proportional to the actual percentages. **d**, Top, Distribution of maximum cross-correlation coefficient across all lick cycle correlated neurons ($n = 242$). Bottom, Distribution of lags for lick cycle correlated neurons. Lag was taken at the time which maximized the cross-correlation coefficient for each neuron. **e**, Two example latSC neurons that are modulated prior to L4. Data are aligned to L4 protrusion onset, and sorted by condition. Within each condition, data are sorted by tip position in the ML plane at L4 protrusion offset. Black bar, analysis window used for GLMs. **f**, GLM schematic. We sought to test whether tongue

position was encoded in pre-contact L4 latSC neuronal activity. Given the close temporal proximity (-120 ms) between past (L3) contact and L4 re-aiming, any relationship we might observe between tongue position and latSC neuronal activity may be confounded by past L3 contact location. We included both variables to test whether L4 tongue position and/or past L3 contact location was encoded in latSC neural activity. Note that, we are using GLMs to examine encoding of tongue position, not as a model of the latSC. **g**, Mean \pm IQR McFadden's pseudo- R^2 across all latSC neurons ($n = 320$ neurons). pseudo- R^2 is a measure of goodness-of-fit for GLMs, with higher values indicating better model fits. Note that pseudo- R^2 values of 0.2–0.4 represent excellent model fits. **h**, Relative contribution of each predictor across all latSC neurons ($n = 320$ neurons). Tip and contact position are separated into their ML, AP or DV components. Error bars represent the bootstrapped IQR. **i**, Percentage of neurons encoding L4 tip position (left) and previous (L3) contact position. Tip and contact position are broken down into neurons encoding only ML, AP or DV components of position, two of these components, or all three.



Extended Data Fig. 10 | latSC photostimulation reveals the same topographic map when conducted in a cued lick task. **a**, Example histological confirmation of latSC photoactivation sites (-3.1 , -3.4 , -3.7 and -3.9 mm AP) and AAV2-hSyn-ChR2 expression (green). Dil and DiD tracts corresponding to a single fibre implant site are orange and purple, respectively. Sites were excluded if fibre tracts were outside of the latSC or in regions with little viral expression (white, in contrast to yellow). **b**, Schematic of experimental timeline. Two latSC photostimulation sites were probed per session, with two trial blocks each. In block 1, mice performed ~ 120 trials of a cued lick task, where no laser trials (Cue only) were interleaved with latSC photostimulation trials (Stim w/cue, Methods). In block 2, mice were photostimulated (Stim only) with no task structure (40 trials). This was repeated for each site on each day. **c**, Trial structure for Stim w/cue (top) and Stim only (bottom). Red and cyan dashed lines are cue and laser onset, respectively. Cyan bar indicates photostimulation duration. Black pulse trains indicate lick duration for each lick. **d**, Polar plots of L1 protrusion endpoints for an example left (left) and right latSC (right) photostimulation session in the 'Stim w/cue' condition. Colours as in **a**. **e**, latSC-evoked L1 protrusion angles similarly depended on latSC photostimulation site in a cued lick task ($n = 8$ mice, left). Black line and coloured dots are median \pm IQR across mice for each stimulation site. Grey lines are individual mice. Right, R^2 for the observed correlation between photostimulation site and L1 protrusion angle (black) compared to shuffled data (grey) for the 'Stim w/cue' condition. $^{**}p < 0.01$, two-sided shuffle test. **f-g**, L1 protrusion probability (**f**) and protrusion latency (**g**) did not significantly differ in post-hoc tests between latSC stimulation sites for the 'Stim w/cue' and 'Cue only' conditions. Kruskal-Wallis test. **h-m**, Lick kinematics during latSC photostimulation for each condition. L1 protrusion latency (**h**), L1 duration (**i**), the L1-L2 ILI (**j**), L1 pathlength (**k**), peak L1 speed (**l**) and the number of acceleration peaks in L1 (**m**) are shown for all trial types. Note that protrusion latencies were briefer and licks were slightly slower following latSC stimulation than with a cue alone. *corrected $p < 0.05$, **corrected $p < 0.01$, two-sided hierarchical bootstrap test; n.s., not significant. Exact statistics are in Supplementary Tables 14, 15.

Reporting Summary

Nature Portfolio wishes to improve the reproducibility of the work that we publish. This form provides structure for consistency and transparency in reporting. For further information on Nature Portfolio policies, see our [Editorial Policies](#) and the [Editorial Policy Checklist](#).

Statistics

For all statistical analyses, confirm that the following items are present in the figure legend, table legend, main text, or Methods section.

n/a Confirmed

- The exact sample size (n) for each experimental group/condition, given as a discrete number and unit of measurement
- A statement on whether measurements were taken from distinct samples or whether the same sample was measured repeatedly
- The statistical test(s) used AND whether they are one- or two-sided
Only common tests should be described solely by name; describe more complex techniques in the Methods section.
- A description of all covariates tested
- A description of any assumptions or corrections, such as tests of normality and adjustment for multiple comparisons
- A full description of the statistical parameters including central tendency (e.g. means) or other basic estimates (e.g. regression coefficient) AND variation (e.g. standard deviation) or associated estimates of uncertainty (e.g. confidence intervals)
- For null hypothesis testing, the test statistic (e.g. F , t , r) with confidence intervals, effect sizes, degrees of freedom and P value noted
Give P values as exact values whenever suitable.
- For Bayesian analysis, information on the choice of priors and Markov chain Monte Carlo settings
- For hierarchical and complex designs, identification of the appropriate level for tests and full reporting of outcomes
- Estimates of effect sizes (e.g. Cohen's d , Pearson's r), indicating how they were calculated

Our web collection on [statistics for biologists](#) contains articles on many of the points above.

Software and code

Policy information about [availability of computer code](#)

Data collection	Custom Labview 2017 code was used to collect behavioral task data, and licensed software from Phantom (PCC 3.4) was used for video collection.
Data analysis	Custom MATLAB 2023b and Python 3.7.11 code was used to analyze the data in this study. Code for analysis can be found here: https://github.com/GoldbergLab/Ito-Gao-et-al-2024

For manuscripts utilizing custom algorithms or software that are central to the research but not yet described in published literature, software must be made available to editors and reviewers. We strongly encourage code deposition in a community repository (e.g. GitHub). See the Nature Portfolio [guidelines for submitting code & software](#) for further information.

Data

Policy information about [availability of data](#)

All manuscripts must include a [data availability statement](#). This statement should provide the following information, where applicable:

- Accession codes, unique identifiers, or web links for publicly available datasets
- A description of any restrictions on data availability
- For clinical datasets or third party data, please ensure that the statement adheres to our [policy](#)

Data are deposited in the Open Science Framework repository: DOI 10.17605/OSF.IO/FY7J5

Research involving human participants, their data, or biological material

Policy information about studies with [human participants or human data](#). See also policy information about [sex, gender \(identity/presentation\), and sexual orientation](#) and [race, ethnicity and racism](#).

Reporting on sex and gender	<input type="text" value="N/A"/>
Reporting on race, ethnicity, or other socially relevant groupings	<input type="text" value="N/A"/>
Population characteristics	<input type="text" value="N/A"/>
Recruitment	<input type="text" value="N/A"/>
Ethics oversight	<input type="text" value="N/A"/>

Note that full information on the approval of the study protocol must also be provided in the manuscript.

Field-specific reporting

Please select the one below that is the best fit for your research. If you are not sure, read the appropriate sections before making your selection.

Life sciences Behavioural & social sciences Ecological, evolutionary & environmental sciences

For a reference copy of the document with all sections, see nature.com/documents/nr-reporting-summary-flat.pdf

Life sciences study design

All studies must disclose on these points even when the disclosure is negative.

Sample size	No statistical methods were used to predetermine sample sizes. We ensured that they were similar to those generally employed in the field and within ethical constraints. Relevant citations for similar sample sizes include: Li et al. (2015), Nature; Inagaki et al. (2019), Nature; Gao et al. (2018), Nature; Seo et al. (2019), Science.
Data exclusions	Data from optogenetic and electrophysiology experiments were excluded if the fiber or probe tract was found to be implanted outside of the brain region of interest after post-hoc histological verification of the implant site.
Replication	Experiments were executed repeatedly within the sample-size constraints generally employed in the field to establish reproducibility. Surgeries and experiments were typically performed in multiple (typically 2 - 3) independent cohorts and the results were reproducible across cohorts.
Randomization	Animals were allocated randomly.
Blinding	Spike sorting for electrophysiological data was performed blind to trial type. For all other experiments/analyses, investigators were not blinded to group allocation, as there were no groupings - conditions (e.g., left/center/right, laser on/off, etc.) were randomly interleaved for the same animals within the same behavioral session.

Reporting for specific materials, systems and methods

We require information from authors about some types of materials, experimental systems and methods used in many studies. Here, indicate whether each material, system or method listed is relevant to your study. If you are not sure if a list item applies to your research, read the appropriate section before selecting a response.

Materials & experimental systems		Methods	
n/a	Involved in the study	n/a	Involved in the study
<input type="checkbox"/>	<input checked="" type="checkbox"/> Antibodies	<input checked="" type="checkbox"/>	<input type="checkbox"/> ChIP-seq
<input checked="" type="checkbox"/>	<input type="checkbox"/> Eukaryotic cell lines	<input checked="" type="checkbox"/>	<input type="checkbox"/> Flow cytometry
<input checked="" type="checkbox"/>	<input type="checkbox"/> Palaeontology and archaeology	<input checked="" type="checkbox"/>	<input type="checkbox"/> MRI-based neuroimaging
<input type="checkbox"/>	<input checked="" type="checkbox"/> Animals and other organisms		
<input checked="" type="checkbox"/>	<input type="checkbox"/> Clinical data		
<input checked="" type="checkbox"/>	<input type="checkbox"/> Dual use research of concern		
<input checked="" type="checkbox"/>	<input type="checkbox"/> Plants		

Antibodies

Antibodies used	mouse anti-NeuN antibody conjugated with Alexa Fluor 555 (EMD Millipore MAB377A5, 1:250 dilution)
Validation	From manufacturer: Demonstrated to react with Rat and Mouse. Unconjugated Anti-NeuN has been shown to work with multiple species including Human, Ferret, Chicken, and Avian. Evaluated by Immunocytochemistry in rat E18 primary cortex cells, as well as Immunohistochemistry. Relevant citations that use this antibody include: Topper et al. (2015), Journal of neuroinflammation; Fowler et al. (2014), PloS one; Fowler et al. (2012), The Journal of biological chemistry.

Animals and other research organisms

Policy information about [studies involving animals](#); [ARRIVE guidelines](#) recommended for reporting animal research, and [Sex and Gender in Research](#)

Laboratory animals	Adult male and female mice (10 - 24 weeks old) were obtained from Jackson Labs. The strains used were VGAT-ChR2-eYFP (JAX# 014548), Vgat-ires-cre (JAX# 028862), Ai14 (JAX #007914), and C57BL/6J (JAX #000664). Ambient temperature in housing was maintained at 72 degrees Fahrenheit, and relative humidity was maintained at 50%.
Wild animals	No wild animals were used in this study.
Reporting on sex	Male and female mice (50% each) were used in all experiments throughout this study, and were assigned randomly.
Field-collected samples	No field-collected samples were used in this study.
Ethics oversight	All experiments were carried out in accordance with NIH guidelines and were approved by the Cornell Institutional Animal Care and Use Committee.

Note that full information on the approval of the study protocol must also be provided in the manuscript.

Plants

Seed stocks	N/A
Novel plant genotypes	N/A
Authentication	N/A